Pure Appl. Geophys. 171 (2014), 59–85

DOI 10.1007/s00024-012-0582-5

Pure and Applied Geophysics

Roundhouse (RND) Mountain Top Research Site: Measurements and Uncertainties for Winter Alpine Weather Conditions

I. GULTEPE,[1] G. A. ISAAC,[1] P. JOE,[1] P. A. KUCERA,[2] J. M. THERIAULT,[3] and T. FISICO[4]

Abstract—The objective of this work is to better understand and summarize the mountain meteorological observations collected during the Science of Nowcasting Winter Weather for the Vancouver 2010 Olympics and Paralympics (SNOW-V10) project that was supported by the Fog Remote Sensing and Modeling (FRAM) project. The Roundhouse (RND) meteorological station was located 1,856 m above sea level that is subject to the winter extreme weather conditions. Below this site, there were three additional observation sites at 1,640, 1,320, and 774 m. These four stations provided some or all the following measurements at 1 min resolution: precipitation rate (PR) and amount, cloud/fog microphysics, 3D wind speed (horizontal wind speed, U_h; vertical air velocity, w_a), visibility (Vis), infrared (IR) and shortwave (SW) radiative fluxes, temperature (T) and relative humidity with respect to water (RH_w), and aerosol observations. In this work, comparisons are made to assess the uncertainties and variability for the measurements of Vis, RH_w, T, PR, and wind for various winter weather conditions. The ground-based cloud imaging probe (GCIP) measurements of snow particles using a profiling microwave radiometer (PMWR) data have also been shown to assess the icing conditions. Overall, the conclusions suggest that uncertainties in the measurements of Vis, PR, T, and RH can be as large as 50, >60, 50, and >20 %, respectively, and these numbers may increase depending on U_h, T, Vis, and PR magnitude. Variability of observations along the Whistler Mountain slope (~500 m) suggested that to verify the models, model space resolution should be better than 100 m and time scales better than 1 min. It is also concluded that differences between observed and model based parameters are strongly related to a model's capability of accurate prediction of liquid water content (LWC), PR, and RH_w over complex topography.

Key words: Extreme winter weather, visibility, snow precipitation, variability of measurements, measurement uncertainty, model validations.

1. Introduction

Numerical weather predictions (NWP) of the meteorological and environmental parameters of important weather events are strongly related to the time and space resolutions, initial conditions and data assimilation techniques. Over mountainous environments where model grids may not match the height changes because of quickly changing environmental conditions, measurements may include large uncertainties and variability; affecting the assessment of NWP model simulations.

The most difficult issue in assessing weather conditions over rough topography is to resolve the natural variability over short distances along the mountain slopes. It is well known that precipitation amount may increase or decrease with height, depending on how the thermodynamical conditions are distributed along mountain slopes (ISAAC *et al.*, 2012; GULTEPE and ZHOU, 2012; MO *et al.*, 2012). When the observations of precipitation type, amount, and phase changes along the mountain are limited, it is very difficult to assess model based predictions. Previous studies suggested that the lower the model resolution, the lower the precipitation amount, and the intensity of model based forecast precipitation rate decreases with increasing grid area size (MAILHOT *et al.*, 2012). They suggested that sampling strategies are important for model validation studies. This work showed that precipitation assessment using the model simulations should be done with the appropriate time and space scales, resolving the physical processes.

---

[1] Cloud Physics and Severe Weather Research Section, Environment Canada, Toronto, ON M3H 5T4, Canada. E-mail: ismail.gultepe@ec.gc.ca

[2] Research Applications Laboratory, National Center for Atmospheric Research, PO Box 3000, Boulder, CO, USA.

[3] Departement des sciences de la Terre et de l'atmosphere, Universite du Quebec a Montreal, Case postale 8888 Succursale Centre-ville, Montreal, QC H3C 3P8, Canada.

[4] University of Manitoba, Winnipeg, MA, Canada.

Birkhäuser

Uncertainty in the measurements of precipitation and visibility (Vis) is strongly dependant on particle density and definition of snow type as a function of temperature usually (Brandes *et al.*, 2007; Gultepe *et al.*, 2012). Although temperature (T) is an important factor in defining particle type and density, relative humidity with respect to water ($\mathrm{RH_w}$) and flow conditions also play an important role for particle shape and density estimation. Visibility estimated directly from particle spectra can include large uncertainties related to assumptions used for distinguishing particle shape. On the other hand, based on direct extinction of light (Gultepe and Milbrandt, 2011), Vis measurements can represent various particle shapes very well but a detailed particle spectra measurement is needed to relate Vis to particle shape and density. Although Vis measurements can be obtained accurately, precipitation rate (PR) measurements for snow may not be obtained accurately because of instrument issues. This suggests that selection of Vis and PR from various instruments should be done carefully. In the case of the Vaisala FD12P sensor, T between -3 and $+6$ °C was defined for the wet snow conditions that may not be valid for NWP model parameterizations for snow (Gultepe and Milbrandt, 2011).

The FD12P T sensor doesn't represent outside air T but air T in the protected cylinder that results in a severe assessment issue for distinguishing snow type. The total precipitation sensor (TPS) PR may include large uncertainties when they are used in mountainous areas with strong turbulence conditions (Rasmussen *et al.*, 2011). Gultepe *et al.* (2012) suggested Vis and precipitation measurements can be highly suspicious when T goes down below -30 °C because they are not calibrated for the cold temperatures. These studies suggest that measurements of meteorological parameters over the mountainous regions create challenging issues for meteorologists and researchers.

Rasmussen *et al.* (2011) provided a detailed summary of snow precipitation measurements. They stated that the estimation of snowfall rate remains one of the most challenging measurements to make because of the wide variety of snow types, shapes, size distributions, and particle densities. This is especially true for ground-based measurements using gauges (Goodison *et al.*, 1989; WMO/CIMO, 1985; Yang *et al.*, 1998, 2001). The weighing gauges weigh the accumulated snow in a bucket and use a glycol-based solution to prevent evaporation of water. Using gauges, PR is typically estimated using the amount of accumulation over a period of $\sim$5–10 min. The Geonor weighing gauges, that use three transducers for measuring snow mass amount, are sensitive to vibration resulting from the wind effects (Thériault *et al.*, 2012). Optical gauges (Gultepe and Milbrandt, 2010) that usually use a laser light, accurately measure particle volume, and perform well for rain. The Vaisala FD12P has combined an optical sensor with a simple measure of snow-water content obtained using a heated plate to provide improved snow estimates (Gultepe *et al.*, 2012).

In the previous studies, T and $\mathrm{RH_w}$ measurements were found to be highly correlated with wind speed (U_h) and solar radiative fluxes (Huwald *et al.*, 2009). Although manufacturers provide low uncertainties for T and $\mathrm{RH_w}$ values, e.g. $+1$ and 5 %, respectively, these can be much larger in cold, windy, and changing moisture conditions (Gultepe and Starr, 1995). During the Fog Remote Sensing and Modeling-Ice Fog (FRAM-IF) project which took place at Yellowknife Airport NWT (North West Territories) for the winter of 2010–2011, $\mathrm{RH_w}$ uncertainty reached up to 20 % (Gultepe *et al.*, 2012). These uncertainties in the basic thermodynamic parameters can pose a serious challenge for assessing model simulations along short distances (<100 m) over mountainous regions (Bailey *et al.*, 2012).

Variability of meteorological parameters observed over mountainous regions is usually very large (Gultepe *et al.*, 2012). Using only surface in situ observations is not sufficient to represent the weather conditions along the horizontal and vertical dimensions; some remote sensing observations to capture environmental variability in the horizontal and vertical distances are also needed. For example, a profiling microwave radiometer (PMWR), microwave rain radar (MRR), and ceilometer as well as a scanning C-band radar were also help to better understand weather conditions in the horizontal and vertical scales (Gultepe *et al.*, 2009; Joe *et al.*, 2012). A PMWR provided T, q_v (vapor mixing ratio), $\mathrm{RH_w}$, and liquid water content (LWC) in a profiling mode

(Bianco *et al.*, 2005) but it needs to be validated using in situ observations; this may be a challenge for stratiform clouds because of a weak signal compared to that of convective cloud systems. All these remote sensing platforms are needed to further assess the weather variability over the mountainous regions.

An overview of the measurements made during the Science of Nowcasting Winter Weather for the Vancouver 2010 Olympics and Paralympics (SNOW-V10) project was given by Joe *et al.* (2012) while the objectives of the overall project were summarized by Isaac *et al.* (2012). The present work focuses on the extensive measurements of fog, precipitation from weighing and optical gauges, particle spectra from 0.3 μm up to cm size, visibility, as well as other meteorological measurements such as 3D turbulence and solar radiation collected at the mountain top called the Roundhouse (RND at 1,856 m) and these measurements, representing extreme weather conditions, are given in next section.

The goals of this work are (1) summarize the instruments and their measurements for the Roundhouse (RND) site on Whistler Mountain, (2) show the variability and uncertainty in the precipitation type and amount, (3) show the response of the sensors to the temperature, wind, and solar radiation changes for various weather events (e.g. cases studies), and (4) emphasize the particle shape effect on precipitation rate estimation and discuss the variability of measurements over a fast changing altitude (e.g. ∼500 m) and extreme weather conditions. There were no reference precipitation measurements as described in World Meteorological Organization (WMO) technical notes because of extreme weather conditions. The following sections will focus on RND instruments, analysis of the observations, results, discussion on uncertainty and variability, and conclusions.

2. *Roundhouse (RND) Meteorological Observations*

In this study, we will focus on the RND instruments and their observations collected during January–April 2010, representing extreme weather conditions such as high winds and turbulent conditions, blowing snow, and freezing precipitation. Figure 1 shows the locations of RND, VOA (Whistler Mountain high level), VOL (Whistler Mountain mid-level), VOT (Whistler Mountain timing flat), TFT (Whistler timing flat), and VOC (Nesters) stations. The symbols and acronyms used in the text are defined in the "Appendix". To show the variability and scale dependency of PR and Vis, the measurements of the FD12P as well as T, $\mathrm{RH_w}$, and wind speed from the all mentioned sites are also used in the analysis. The heights of RND, VOA, VOL, VOT, and TFT are, respectively, 1,856, 1,640, 1,320, 805, and 776 m.

Figure 1b shows the RND site and instrumented towers around the RND site. There were three towers, called tower 1 (T1), T2, and T3. Table 1 shows the list of the sensors and their definitions used in the towers. The main observations collected at RND were related to T, $\mathrm{RH_w}$, horizontal and vertical air speed (U_h and w_a), radiative fluxes, 8 Hz 3D wind speed and direction, particle spectra from disdrometers (LPM, OTT), Rosemount icing detector (RID) signal, precipitation type, amount, and rate (FD12P and HSS-VPF-730), particle video imaging (PVI), snow and droplet spectra, and particle shape (GCIP, FMD, snow photography), visibility (FD12P, HSS-VPF-730, Sentry), aerosol spectra (>0.3 μm at 8 channels, CAP) and short wave radiative fluxes (SWRF) (SPN1 and Eppley radiometers), snow amount and rate [Geonor and TPS (total precipitation sensor)], and radar reflectivity (MRR). The other measurements (Joe *et al.*, 2012) were available from the remote sensing platforms (e.g. PMWR and MRR) located at the TFT (Timing Flats, 776 m), and Whistler Doppler Radar located at (VVO, 557 m). Radiosonde balloons were released from the VOC (Nesters, 651 m).

Because of the RND location, the measurements represent extreme weather conditions. There was no WMO suggested reference site for precipitation, as a double fenced intercomparison reference (DFIR) shield installation was not possible at any location along the Whistler mountain slope. Snow gauge shields were not used due to wet snow capping issues. The site was significantly affected by strong winds and turbulence, making measurements very difficult during extreme weather conditions such as blowing snow, freezing precipitation, and cold temperatures.

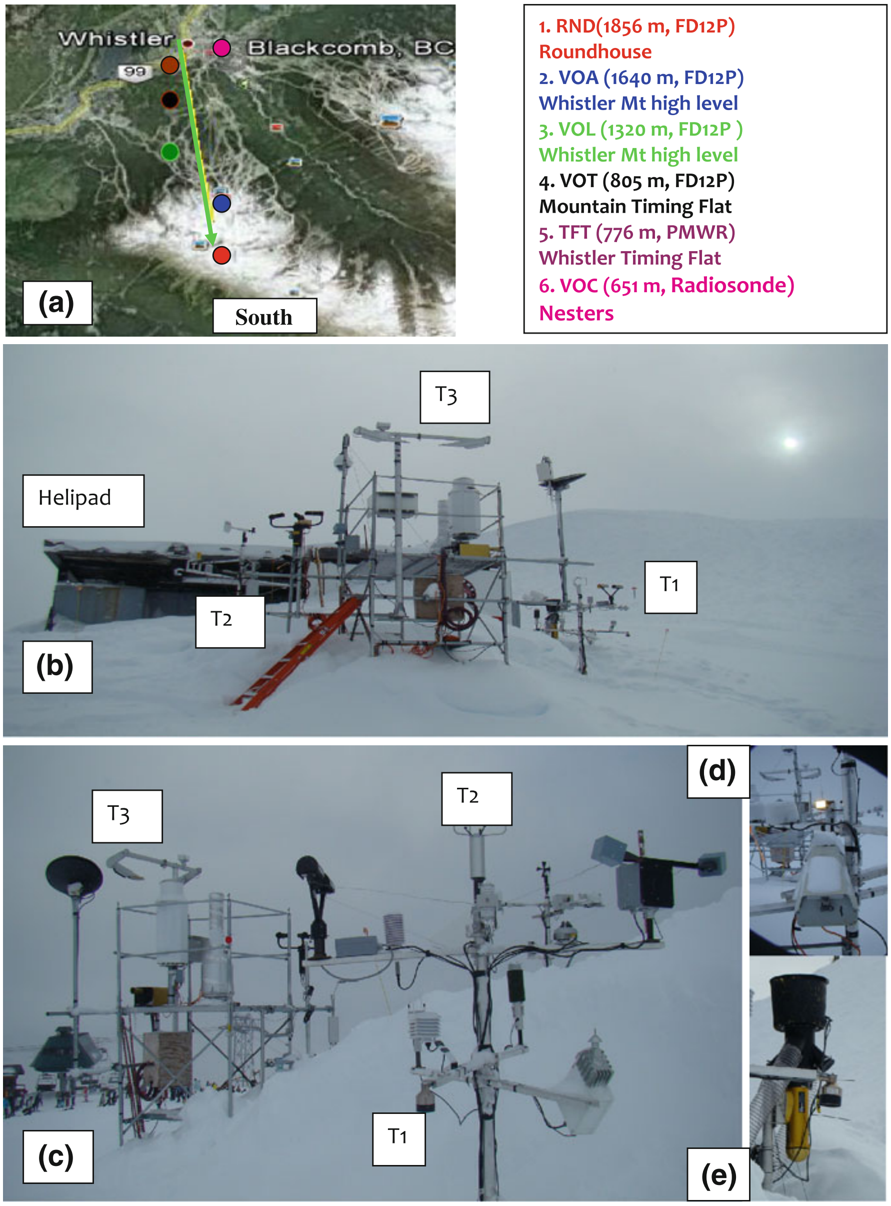

Figure 1
Shows the project sites over the Whistler Mountain: a topographic map (**a**) with stations along the mountain slope. The *green line* shows the path of the Whistler Gondola. The major instrumented sites were shown in (**b**), and instrumented towers are shown in (**c**). The FD12P is the Vaisala all weather present sensor and measured precipitation rate, amount, and visibility at 1 min sampling intervals. It was available over the all major stations. Pictures of PVI and GCIP are shown in (**d**) and (**e**), respectively

The Geonor is an operationally used sensor. The TPS is a relatively new instrument and its response to strong wind environments was tested. Note that the TPS precipitation algorithm uses a collection efficiency correction as a function of wind speed. Many sensors had difficulty operating properly when blowing snow and freezing precipitation occurred. Solar radiation effects were large on T and RH_w measurements and they are summarized in discussion section.

All the measurements were collected with an identical pair of sensors in case one of them failed or

Table 1

The instrument list and their specific characteristics as well as their location at the site (Fig. 1) RND-L and RND-R represent the left and right directions, respectively, of the RND's north direction

Instrument	Measurement	Characteristics	Location
(1) FMD fog monitor	Droplet/ice spectra	<50 µm	T3
(2) GCIP probe	Droplet/ice spectra	15–960 µm	RND-L
(3) OTT parsivel	Particle spectra	400-max	T1
(3) CAP aerosol	Droplet/aerosol spectra	0.3–10 µm; 8 chan.	T1
(4) Geonor	Precip rate/amount	>0.1 mm h^{-1}	T3
(5) YU IPC	Particle spectra	15–500 µm	T2
(6) FD12P Vis	Vis/precip amount	0.1 mm/h	T3
(7) Sentry Vis	Vis	>10 m	T3
(8) DMIST camera	Vis and images, extinction	For warm fog	RND-R
(9) YES TPS	Precip amount	0.25 mm/h	T3
(10) VRG101	Precip amount	0.5 mm/h	T3
(11) DSC111	Precip amount/friction	Surface phase	T1
(12) DST111	Surface temperature	Surface T/dew point	T1
(13) HMP45C	RH and T	At 4 m	T2
(14) HMP45C212	RH and T	At 4 m	T1
(15) WXT520	T, RH, 2D wind, Pressure, Precip.	At 4 m	T1
(16) SR50AT	Snow depth	−45 to 50 °C	T1
(17) Eppley IR/SW	Broadband radiative fluxes	10 %	T2
(18) Campbell RH/T(2)	RH and T	10 % and ±1C	T1 and T2
(19) Young Ultra 3D anemometer	3D wind and turbulence	4–32 Hz samp. rate	T1
(20) SPN1	Dir, Diff radiation, cloud cover	0.4–2.7 µm	T1
(21) MRR	Rain size spectra, PR, Z	For rain/snow	T3
(22) RID	Icing rate	Icing amount	T1
(23) Vaisala WXT	P, T, wind, PR	PR for rain	T1
(24) CRN1	IR and SW BRF	0.2–3 µm	HT1
(25) HSS VPF-730	Visibility/present weather	>0.1 mm/h	T3
(26) LPM 5.4110	Particle spectra	0.1 mm–cm, 22 ch	T1
(27) Axis Camera	3D picts	Zoom/regular	T3
(28) PVI (NCAR)	Snow shape and spectra	>0.5 mm	T2–T3
(29) Snow photography	Particle shape	>100 µm	RND
(30) Young 2D anemometer	2D wind speed and direction	>10 %	T2

The instrument acronyms are given as: *FMD* fog measuring device, *GCIP* ground cloud imaging probe, *CAP* climatronic aerosol profiler, *YU IPC* York University ice particle counter, *TPS* total precipitation sensor, *LPM* laser precipitation sensor, *PVI* particle video imaging, and *RID* Rosemount icing detector

to assess their responses in various environmental conditions. The sensors were calibrated at RND and also at EC (Environment Canada) before the deployment. The visibility sensors were calibrated in the field using the calibration kits and procedures for that instrument. The precipitation sensors were tested using a known mass of water, for example, by pouring water into the weighing gauges. The sensors used for T and RH_w were newly purchased and were factory calibrated. They were also checked using recommended procedures for possible issues after the project. If the sensors were not heated, errors due to freezing precipitation could affect measurements significantly such as wind measurement observed with the Young 3D wind sensor during wet snow and icing conditions. These conditions were identified using a RID sensor which responds to icing conditions.

3. Analysis and Instrumental Issues

Analysis of observations were performed by examining: (1) time series of various meteorological and thermodynamical measurements, (2) scatter plots of the same parameters from identical two sensors to assess the bias, (3) wind and SWRF effects on T, RH_w, and precipitation rate, and (4) Vis versus PR plots to show the variability for the various particle shapes. Then, PR, Vis, T, RH$_\mathrm{w}$, and wind speed (U_h) values from the three stations (RND, VOA, and VOL) were averaged to represent the 0.5 km horizontal scale (slope ~0.7 km).

In the analysis, the five cases with three major events, representing: (1) blowing snow (BSN) conditions, (2) snow (SN) conditions, and (3) freezing fog (FF) and icing (ICNG) conditions, were examined. These conditions are shown in Fig. 2. Note that all these conditions may result in very low Vis conditions. Therefore, in the analysis, their effect on Vis and PR calculations was considered carefully using the laser precipitation monitor (LPM) sensor and wind measurements because their integrated values can be used to assess specific weather events.

The FD12P measurements may include large uncertainties when air T is between −3 and +6 °C during which FD12P based mixed precipitation information may not be true if the upper level conditions do not represent the mixed phase conditions or there is an inversion. Therefore, particle shape recognition at the low levels may not be representative of the true conditions at higher levels (Gultepe *et al.*, 2012). It should also be emphasized that, at sizes less than 500 µm, disdrometers can include large uncertainties and should be used cautiously. During the project, snow particles were collected over plates covered with a piece of cloth (as in Fig. 2d–h) and their pictures were taken directly using a macro lens in the field (Gultepe *et al.*, 2012). Various snow particle shapes and their distributions are shown in Fig. 2 and for splintered snow crystals, e.g. needles (−6 °C, January 28 2010) in box d, sector plates and stellar crystals, and needles in box e (January 28 2010), graupel with riming in box f (March 4 2010), various mixed snow crystals in box g (March 7 2010), and aggregates and stellar crystals in box h (March 9 2010). These images, collected over approximately 1 min time intervals, show that snow crystals had very variable particle shapes and distributions. Clearly, it is shown that particle shape at the surface may not be related to surface T. It should be noted that accurate PR from particle spectra can be obtained only when both snow and ice particle characteristics such as shape, concentration, cross-section area and fall velocity over entire size range are known.

Visibility and PR are obtained from either the present weather sensors or weighing gauges. Both parameters are strongly related to particle shape and density, and these parameters are also related to T and RH$_\mathrm{w}$, and dynamical activity within the clouds and boundary layer. FD12P PR measurements are related to optical characteristics of snow scattering and capacitance measurements of melted snow (SWE). When the melted water amount is used to estimate snow depth, usually a ratio of SWE ~1:10 is used, e.g. 2 mm converts to 20 mm snow physical depth. In this case, Vis versus PR$_\mathrm{SN}$ for snow is plotted for various particle shapes to emphasize the particle shape effects. The LPM PR$_\mathrm{SN}$ (mm h^{-1}) value is obtained using the following equation:

$$\mathrm{PR} = 3,600\left(\frac{\pi}{6}\right)\sum_{i=1}^{m} N_i V_\mathrm{f} D^3 \qquad (1)$$

where V_f is the measured particle fall velocity (mm s^{-1}), N_i the ice crystal number concentration (cm^{-3}), D the diameter (cm) or maximum size of ice snow particles. V_f is determined directly from falling particles through the sampling volume over Δt time period. N_i is calculated as:

$$N_i = \frac{C_i/V_{\mathrm{f},i}}{\mathrm{SA} \times \Delta t}, \qquad (2)$$

where C_i is the count of particles at ith bin, SA the sampling area (45.6 cm^2), and Δt the sampling time period. The fall velocity (cm s^{-1}) is directly obtained from the sensor algorithm. In order to get true snow water equivalent rate, PR$_\mathrm{SN}$ at each bin needs to be multiplied with snow density ($\rho_\mathrm{SN} = \alpha D^\beta$) described by Huang *et al.* (2010) where $\alpha = 0.178$ and $\beta = -0.922$ for wet snow for $D > 1$ mm (Brandes *et al.*, 2007). Huang *et al.* (2010) stated that if N_i is reduced about 50 %, PR$_\mathrm{SN}$ was underestimated at about 34 % with $\alpha = 0.21$ and $\beta = -0.80$. Based on Eq. 2, it is recognized that particle shape effects are included in the PR through the V_f. Note that the coefficients can change depending on snow type. It is clear that particle shape recognition from all disdrometers and FD12P are based on retrievals that may not represent true particle shape statistics. This suggests that without accurate particle shape recognition, water equivalent snow precipitation rate (PR$_\mathrm{SN}$) values may include large uncertainties. In this respect, FD12P

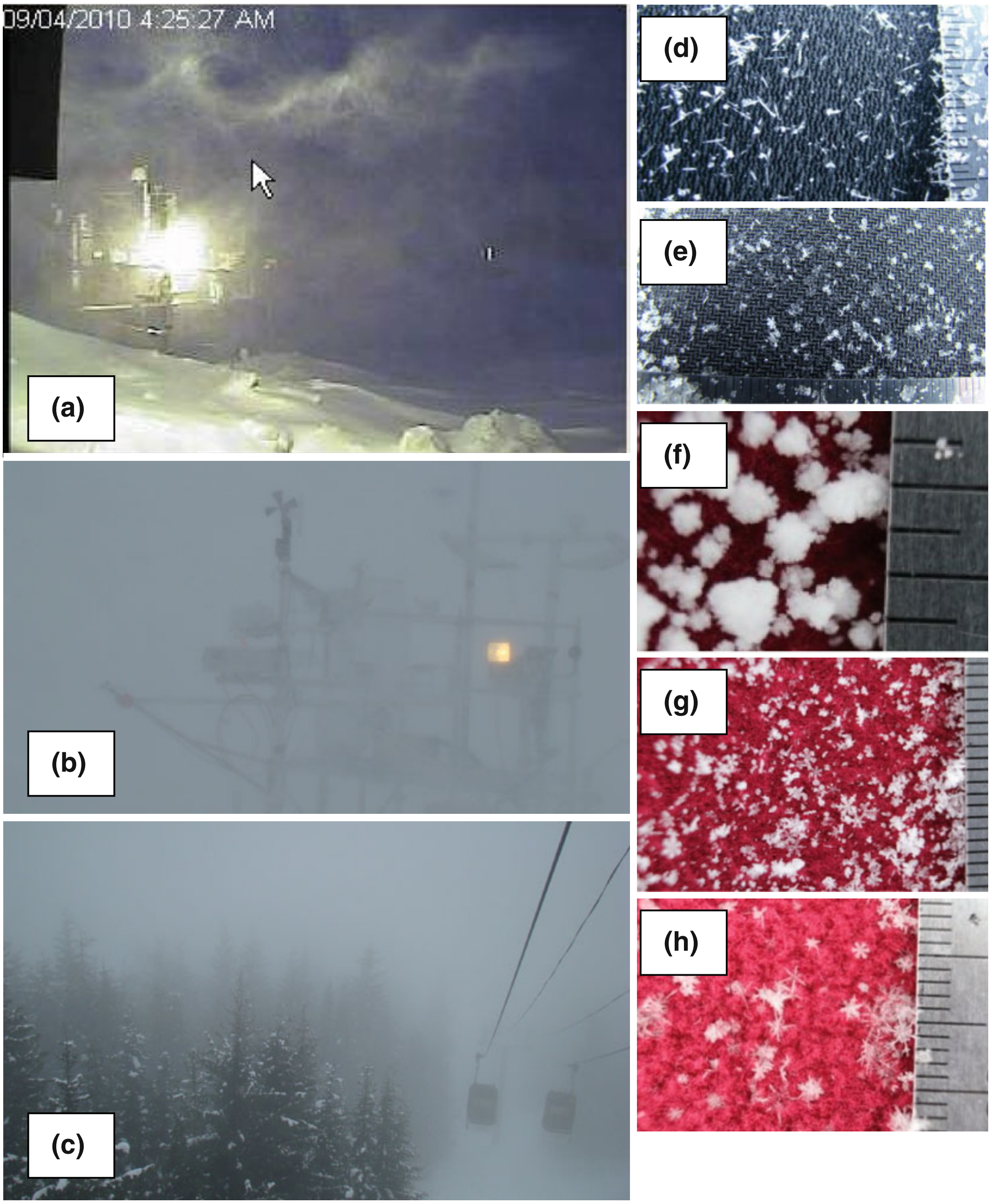

Figure 2
Severe weather events at the RND site: April 9 for blowing snow event (**a**), Jan 28 for heavy snow and low visibility event (**b**), and Jan 25 for heavy freezing fog event at VOA (**c**). Pictures of the various snow crystal types taken by the first author during snow storm conditions: splintering mechanism at −6 °C for Jan 17 2012 (**d**), dendrites and wet particles for Jan 21 (**e**), graupel for Jan 17 (**f**), rimed particles; including dendrites, sector crystals, and some aggregates for Jan 21 (**g**), and light snow with aggregates and stellar crystals for Jan 21 (**h**)

Table 2

Cases used in the analysis: Jan 17 case includes observations from RND, VOA, and VOL that are used to emphasize variability in the measurements along the Whistler mountain slope and discussed in Discussion section. VOT observation were not available on this day

Cases	Precip type	U_h; w_a (m s^{-1})	Max PR (mm hr^{-1})	T(°C); max RH$_w$ (%)	minVis (m)	RID (Icing)
Jan 17	SN; FF	10; 2	3	(−8; 0); 95	50	Yes
Jan 25	SN; FF; BSN	6; 2	5	(−3; −4); 95	200	Yes
Mar 17	LSN; FF	8; 1	3	(−3; −8); 95	150	Yes
Mar 30	LSN; FF	7; 1.5	6	(−5; −8); 95	100	Yes
Apr 5	SN; FF	4; 2	3	(−3; −7); 100	100	Yes

measurements at least use the melted snow amount to estimate PR$_{SN}$.

4. Results

The five cases related to FF and ICNG, BSN, and SN conditions (Table 2) were selected to accomplish the goals of this study. The Jan 17 2010 case is given in Sect. 5 to show the importance of variability in the model validations. The cases are summarized below.

4.1. Case Studies

4.1.1 Jan 25 Case (with FF, BSN, SN, ICNG)

Time series and cross correlation plots of the measurements, and wind effects on PR are shown in Fig. 3. Vis on this day went down to almost 1000 m for several hours (box a). PR from various sensors went up to 3 mm h^{-1} (box b) but significant differences occurred among them. The PR$_{geo}$ from the Geonor sensor had significantly lower value compared to Vaisala FD12P (PR$_{fdp}$) when turbulence and strong winds occurred (e.g. 1800 UTC). The PR$_{tps}$ from the Yankee TPS sensor was usually comparable to PR$_{fdp}$. Maximum U_h and w_a reached 6 and 2 m s^{-1} (box c), respectively, but U_h was usually less than 3 m s^{-1}. Note that strong wind and turbulence significantly affected both PR$_{geo}$ and PR$_{tps}$ measurements because of collection efficiency issues and significant dynamical effects on the plates of the TPS. The Jan 25 case had saturated conditions (RH$_w$ >97 %) for the entire day and this resulted in FF (see Rosemount Icing Detector relative tipping frequencies) over cold temperatures (−3 to −5 °C) (box d).

The PR comparisons shown on Fig. 3e, f are for PR$_{fdp}$ versus PR$_{tps}$, and versus PR$_{geo}$, respectively. When PR <2 mm h^{-1}; relative scattering is very large for both plots. For an example, when PR$_{tps}$ = 1 mm h^{-1}, PR$_{fdp}$ can be between 0.2 and 2 mm h^{-1}. For PR$_{geo}$, this difference can be between 0 and more than 2 mm h^{-1}. Overall, PR varies from case to case. Figure 3g–i show PR$_{tps}$, PR$_{geo}$, and PR$_{fdp}$ versus U_h, respectively. PR$_{tps}$ decreases with increasing U_h; when $U_h > 3$ m s^{-1}, PR decreases significantly (box g). PR$_{geo}$ (box h) also decreases in a similar way. PR$_{fdp}$ (box i) measurements appear to be not affected as much as PR from other precipitation sensors.

The spectral precipitation sensors such as disdrometers can also be used for PR and Vis calculations. Figure 4a–d represent V_f, Vis, and PR$_{lpm}$ from LPM, and V_f from MRR, respectively. Note that the PR estimation obtained using Eq. 1 from LPM measurements does not use counts with sizes <0.1 mm (Fig. 4a). This figure shows V_f versus particle diameter with counts on the color bar. Two areas of particle counts (C) on the plots are important to emphasize; first, $C > 500$ in counts at sizes <0.5 mm in diameter signifies the BSN particles and small snow particles. The green line is the theoretical curve for V_f representing cloud liquid droplets/drops. Second, below the curve, usually snow particles exist. Large snow flakes (diameter >3 mm) are seen with V_f = 0.5–4.2 m s^{-1}. Note that the stronger the vertical air velocity (w_a) snow crystal gets the higher V_f with increasing particle size range.

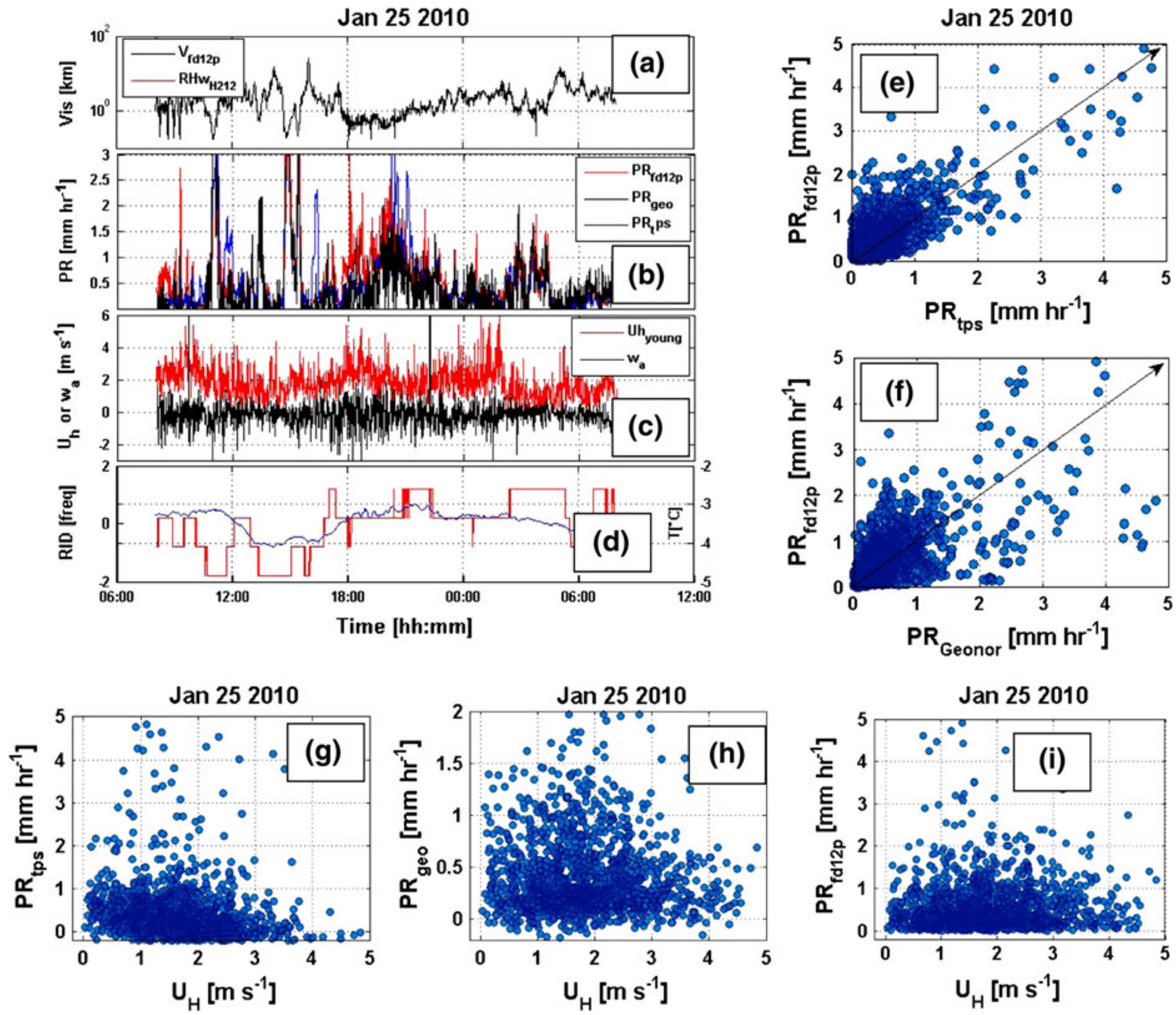

Figure 3

Time series of Vis from FD12P and RH_w from HMP212 °C sensor (**a**), PR from FD12P, Geonor, and TPS (**b**), horizontal (U_h) and vertical wind (w_a) from ultrasonic anemometer (**c**), Rosemount icing detector relative frequency (*red line*) and T (*blue line*) (**d**), PR from FD12P versus PR from TPS (**e**) and versus PR from Geonor (**f**), PR from TPS versus horizontal wind (U_h) (**g**), PR from Geonor versus U_h (**h**), and PR from FD12P versus U_h (**i**) for Jan 25 2010

During fog and snow conditions, Vis_{lpm} went down below 1 km for almost 50 % of time (Fig. 4b). After 6 pm, Vis_{lpm} was below 500 m for about 5 h. The PR_{lpm} was usually less than 5 mm h^{-1} (Fig. 4c) and found to be larger than PR_{fdp} and PR_{geo}. V_f obtained from MRR was between 0.3 and 5 m s^{-1} (Fig. 4d) which was consistent with V_{flpm} (Fig. 4a).

Using the NASA PVI probe (Newman *et al.*, 2009), time series of snow crystal width as a maximum dimension (W) is shown in Fig. 5a; the color bar shows the spectral number concentration density (N_{id}, m^{-3} mm^{-1}). Clearly, W < 1 mm, N_{id} becomes about 5 m^{-3} mm^{-1}. Variability in N_{id} versus diameter (D) is shown in Fig. 5b over 10 min time intervals. For this case, the slope of the spectra did not change much but N_i over 10 min intervals changed significantly for a given D. Figure 5c shows the snow crystal shapes from PVI; including mostly dendrites and aggregates with sizes up to 10 mm.

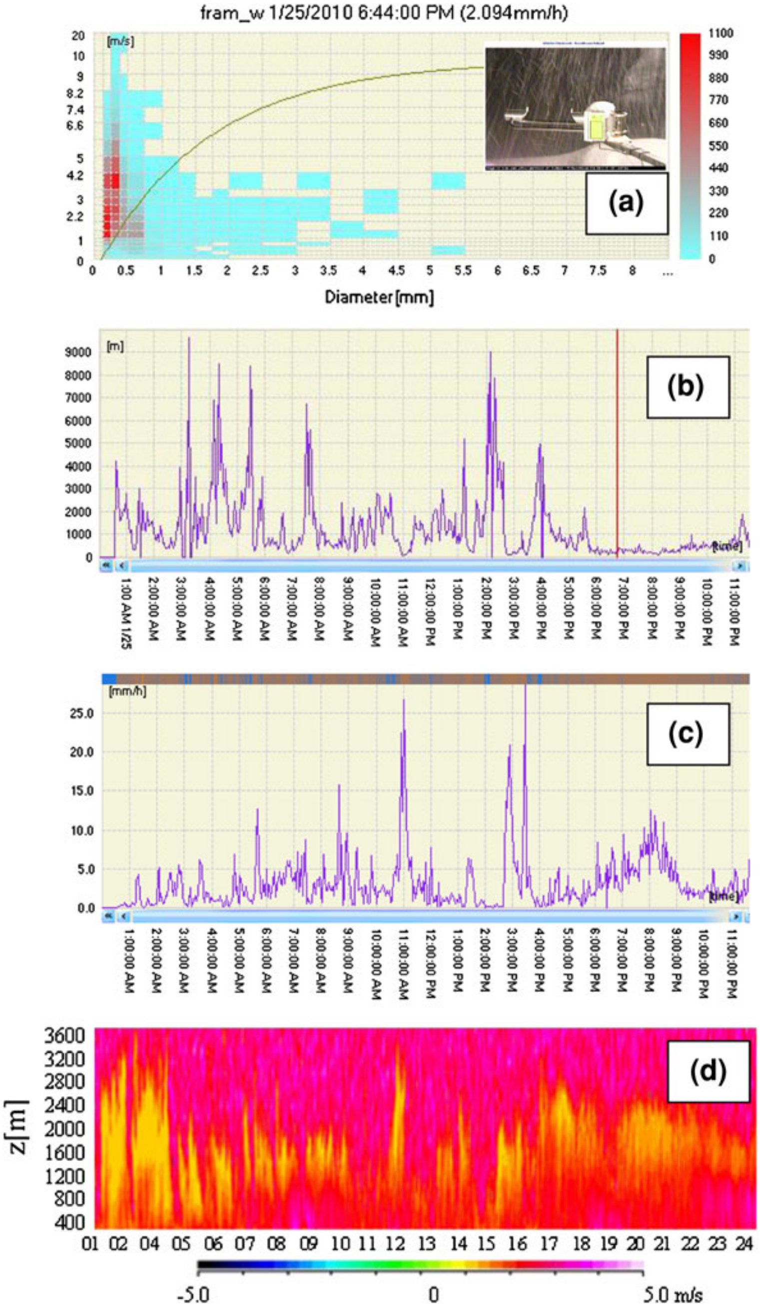

Figure 4

Particle fall velocity (V_f) versus particle width (diameter) (**a**); the *color bar* shows the counts (C) of particles (e.g. snow or droplets). The LPM sensor used for observations is shown in the inlet. Time series of Vis is shown in (**b**). The *vertical red colored line* indicates where the counts in (**a**) is taken. The precipitation rate (PR_{lpm}) time series is shown in (**c**). The MRR particle fall velocities time-height cross section is shown in (**d**). The results are shown for Jan 25 2010

4.1.2 March 17 Case (FF, Strong Gust, Light SN)

The time series plot in Fig. 6 is obtained in a similar way to that in Fig. 3 given for January 25 case study. Vis_{fdp} was less than 1 km for the first 6 h, and then, occasionally, snow showers occurred (box a). PR from various sensors was usually below 0.3 mm h^{-1} (box b) but significant differences occurred among

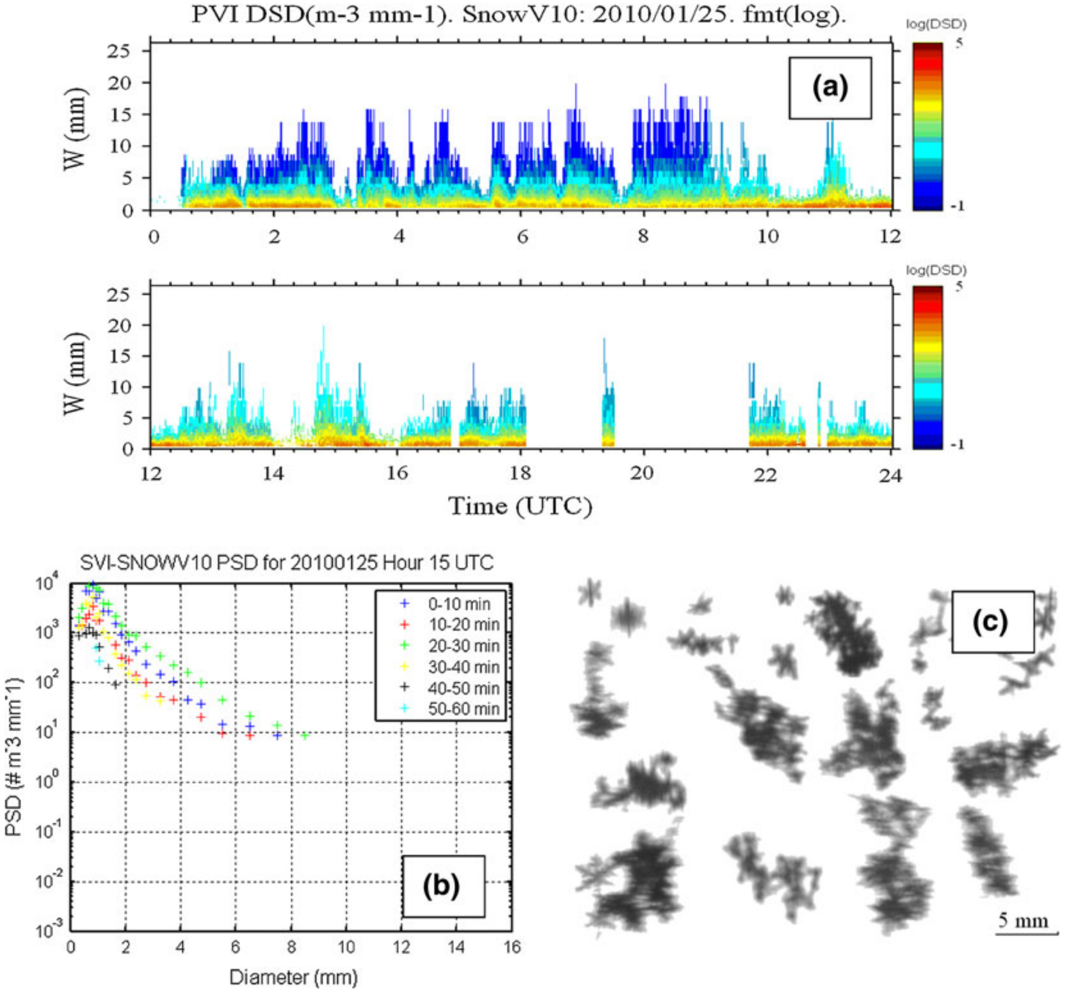

Figure 5

Time series of width (W) of the particles measured with PVI (**a**). The *color bar* indicates the particle number concentration density (N_{id}). The spectra obtained over 10 min intervals are shown on (**b**) and ice crystal images collected during the snow storm at the RND station are shown in (**c**). The results are shown for Jan 25 2010

them. The $\mathrm{PR}_{\mathrm{tps}}$ did not report the observations because of a malfunction. The $\mathrm{PR}_{\mathrm{geo}}$ had significantly larger values as compared to $\mathrm{PR}_{\mathrm{fdp}}$ because of strong turbulence and winds. Therefore, $\mathrm{PR}_{\mathrm{geo}}$ measurements cannot be reliable for PR <0.5 mm h^{-1}. During freezing drizzle events (FDRZ), 3D wind components were not measured accurately before 1200 UTC because the Young ultrasonic sensor was iced up. During non-icing conditions, the U_{h} and w_{a} (vertical air velocity) reached to 8 m s^{-1} and 1 m s^{-1} (box c), respectively. Note that wind speeds, similar to the January 25 case, significantly affected $\mathrm{PR}_{\mathrm{geo}}$ measurements because of collection efficiencies. In this case, saturated conditions (RH_{w} >95 %) until 1800 UTC resulted in FDRZ (see RID tipping relative frequencies) over temperatures from −7 to −12 °C (box d).

The PMWR retrievals (Bianco *et al.*, 2005) for the March 17 case are shown in Fig. 6e where the color bar is for RH_{w}. The T and LWC are shown with light colored solid lines and light colored dotted lines, respectively. Between 0600 and 1800 UTC, icing over sensors at RND (1856 m) was very severe and LWC ~0.16 g m^{-3} based on GCIP measurements was observed at the RND level. The 3D wind sensor during icing event was iced up, resulting in a malfunctioning (Fig. 6c). Just before 0600 UTC, icing was very severe; LWC reached up to 0.3 g m^{-3}.

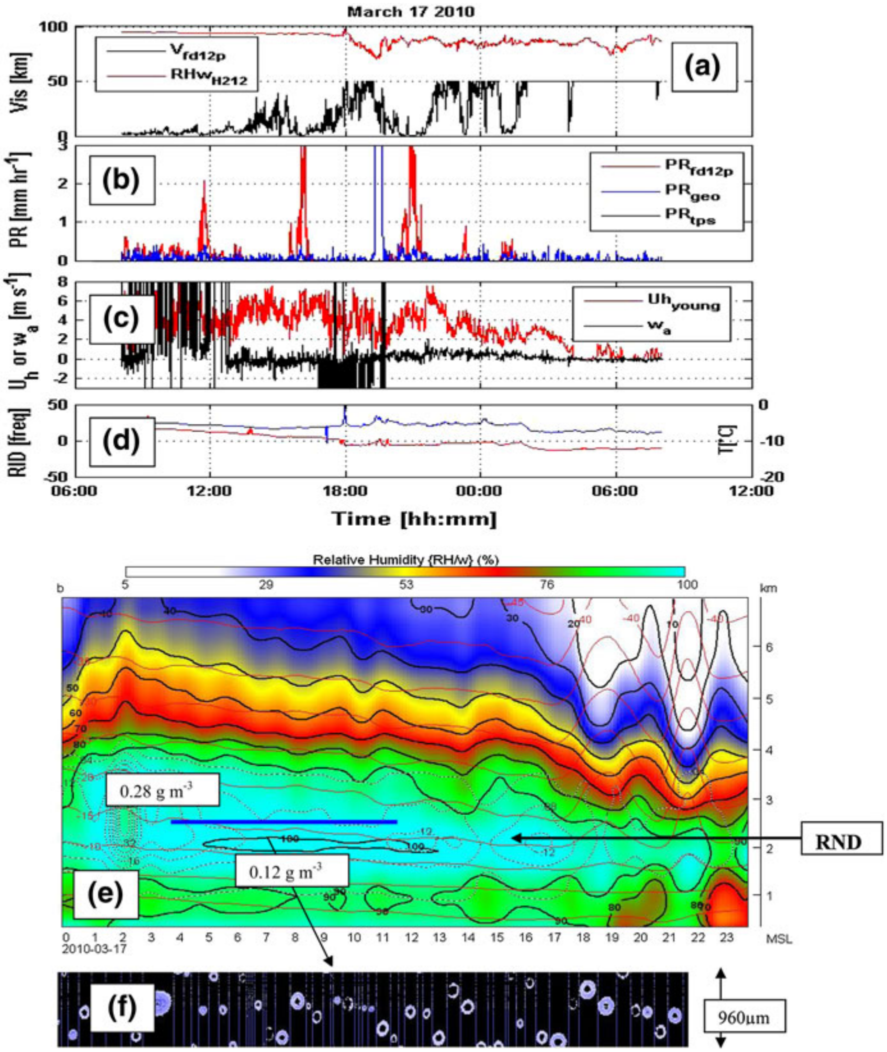

Figure 6

Time series of various measured parameters are shown in box **a**–**d** as given in Fig. 3 but for the March 17 case. In this case, icing conditions are indicated by PMWR measurements (**e**) and shown by *black dashed lines* for LWC. LWC estimated using GCIP data is shown in (**f**). In (**e**), the *blue line* indicates RND level where LWC is measured by both GCIP and PMWR. RH$_w$ and T are shown by colored regions and *solid black lines*, respectively. At RND level, T was about −10 °C

The GCIP images (Fig. 6f) suggested that drop diameters were between 50 and 300 µm. Integration of measurements from various sensors on this day suggested that freezing drizzle and precipitation conditions can occur often at mountainous regions.

4.1.3 March 30 Case (Heavy SN Conditions)

Figure 7 is obtained similar to the previous cases. The Vis$_{\mathrm{fdp}}$ during saturated conditions (RH$_w$ >95 %) came usually down to a few hundred meters during very low PR$_{\mathrm{fdp}}$ (<0.5 mm h^{-1}) measurements (box a). The PR from various sensors reached 3 mm h^{-1} between 1600 and 1800 UTC (box b) but there were significant differences between them. The PR$_{\mathrm{tps}}$ had significantly larger values (∼2 mm h^{-1}) compared to PR$_{\mathrm{fdp}}$ and PR$_{\mathrm{geo}}$ values (<0.5 mm h^{-1}) when U_{h} were more than 4 m s^{-1} (before 1100 UTC). Clearly, TPS sensor was not working accurately on this day when strong winds were occurring. The U_{h} and w_{a} reached to 6 and ±1 m s^{-1} (box c), respectively, that significantly affected PR$_{\mathrm{geo}}$ and PR$_{\mathrm{tps}}$ measurements

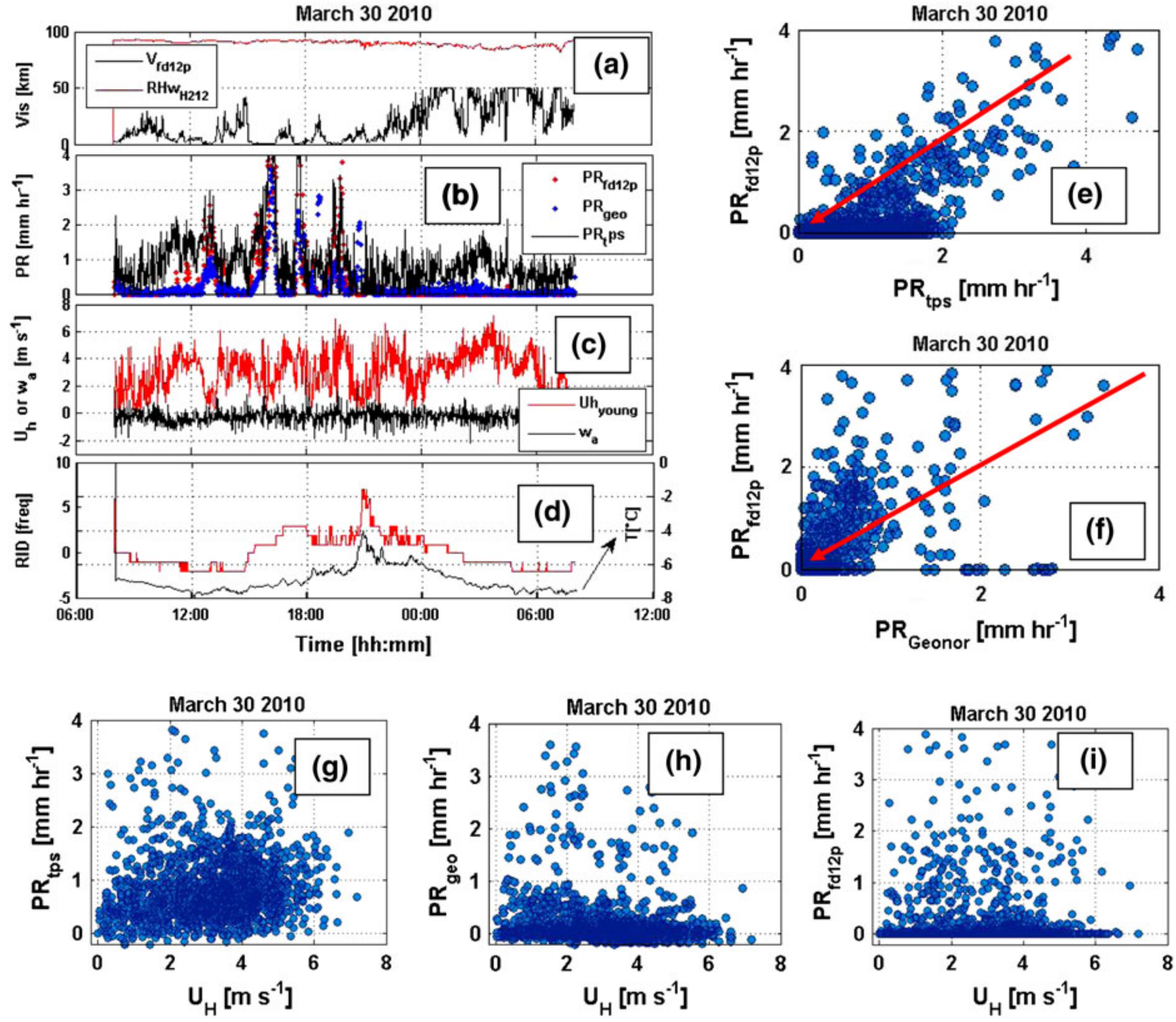

Figure 7
Time series and scatter plots of various measured parameters as given in Fig. 3 but they are for March 30 2010

when PR <0.5 mm h^{-1}. Because of collection efficiency issues of small particles and dynamical effects, both PR_{tps} and PR_{geo} include large uncertainties. On this day, RH_w was usually >95 % for the entire day; FF (see RID tipping relative frequencies) was occurring occasionally over cold temperatures (−5; −8 °C) (box d).

The PR comparisons from Geonor, TPS, and FD12P measurements are shown in Fig. 7e, f. When PR_{tps} <2 mm h^{-1}, PR_{fdp} was usually less than 0.3 mm h^{-1}. For large PR values, PR_{fdp} was larger than PR_{tps}. For an example, when $PR_{tps} = 3$ mm h^{-1} at 1300 UTC, PR_{fdp} was usually less than 2 mm h^{-1}. For PR_{geo} <0.5 mm h^{-1} (1100 UTC), PR_{fdp} was less than 1 mm h^{-1}; this likely reflects the Geonor's slower response to low precipitation rate conditions. Figure 7g–i show PR_{tps}, PR_{geo}, and PR_{fdp} versus U_h, respectively. The PR_{tps} (box g) increases with increasing U_h which is opposite to the PR_{geo} trend (box h) in general. The PR_{geo} decreases (∼50 %) with increasing U_h when $U_h > 2$ m s^{-1}. The PR_{tps} measurements were much larger than both PR_{geo} and PR_{fdp}. The PR_{fdp} (box i) shows no wind dependency.

During the extreme weather conditions, thermodynamical parameters such as RH_w and T can be affected by both SWRF and U_h. Figure 8a–f were

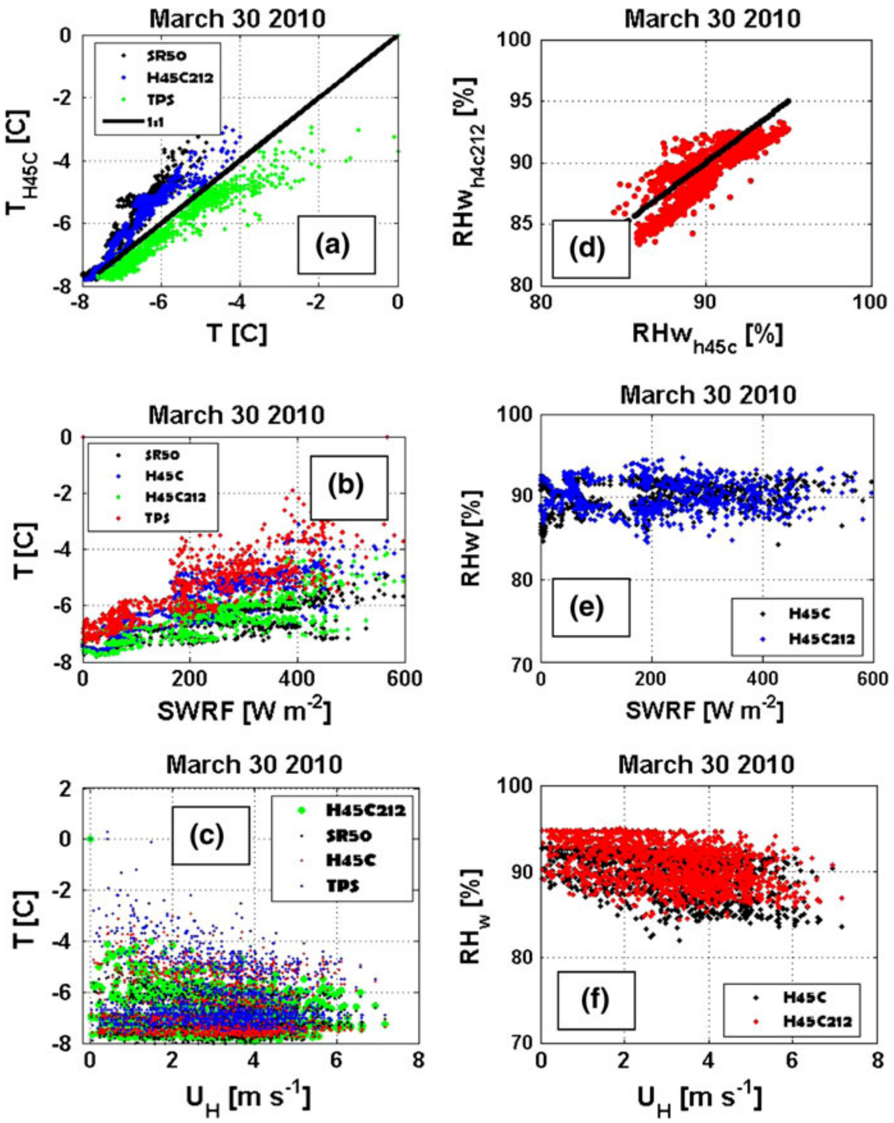

Figure 8

Scatter plots of temperature from HMP45C (T_{h45c}) versus others (T_{sr50}; T_{tps}; and T_{h45c}) (**a**), T_{h45c}, T_{h212}, and T_{tps} versus SWRF (**b**), T from all sensors versus horizontal wind speed (U_h) (**c**), RH_{wh212} versus RH_{w45c} (**d**), RH_{wh45c} versus short wave radiative flux (SWRF) (**e**), and RH_{w45c} and RH_{wh212} versus U_h (**f**) for March 30 2010

obtained for T and RH_w along y axis, respectively. The T_{h45c} from HMP45C versus T_{h212} from HMP45C212, T_{tps}, and T_{sr50} are shown in Fig. 8a. With increasing T, differences between them increase. If we assume that T_{h45c} is correct and its value is -4 °C, then, T_{tps} ~ -3 °C, T_{sr50} ~ -6 °C, and T_{h212} ~ -5.5 °C. Differences decrease when T goes down to -8 °C. Figure 8b shows T versus SWRF. When the sun comes out, T measurements range between -6 and -8 °C (difference ~ 2 °C). A sudden jump in T value about 2 °C at 160 W m^{-2} was likely due to direct solar radiation effect on the sensor shield. This difference rises to 5 °C when SWRF was about 500 W m^{-2}. It seems that both T_{h212} and T_{sr50} were less responsive to SWRF changes, indicating that their shields were more effective for this case. Figure 8c (same parameters as in Fig. 8b) shows various T measurements versus U_h. It seems that T_{tps}, T_{h45c}, and T_{h212} were significantly affected by increasing wind speed, resulting in lowering T from −2 to −6 °C. T_{tps} measurements were affected severely with increasing wind speed compared to other measurements.

The plot of RH_{wh212} versus RHw_{h45c} is shown in Fig. 8d. In this figure, for a given value of RH_{wh45c} ~90 %, RH_{wh212} changes from 87 to 92 %. A 5 % uncertainty in RH_w measurements for this case was found to be reasonable as defined in the company's manual. Figure 8e shows RH_w versus SWRF. For a given SWRF, RH_w from both H45C and H45C212 sensors usually varies between 85 and 93 %. An uncertainty in RH_w measurements is found to be about 8 %. Increasing U_h from 0 to 7 m s^{-1} also resulted in RH_w values ranging between 85 and 95 %. This may be a result of evaporating effects of the wind speed.

4.1.4 April 5 Case (FF, SN)

Results for this case are shown in Figs. 9 and 10. The Vis_{fdp} during light SN and FF conditions was about a few hundred meters for PR <0.5 mm h^{-1} (box a). The PR from the various sensors was less than 3 mm h^{-1} for entire day (box b); the PR_{tps} increased to 2 mm h^{-1} while PR_{fdp} had values less than 0.5 mm h^{-1} between 1800 and 0700 UTC when U_h was about 3–4 m s^{-1}. Clearly, TPS measurements were strongly affected by the intense winds. On this day, the U_h and w_a reached 4 and ±1 m s^{-1} (box c), respectively. RH_w was usually >95 % before 1800 UTC, and decreased to 75 % for very light SN PR. The FF (see tipping RID values) was indicated occasionally with cold T (−2; −5 °C) and saturated RH_w (box d).

The PR inter-comparisons from TPS, Geonor, and FDP measurements are shown in Fig. 9e, f. When PR_{tps} <2 mm h^{-1}, PR_{fdp} was usually less than 0.5 mm h^{-1}. For large PR values, PR_{fdp} was usually less than PR_{tps} but not always. For $PR_{tps} = 3$ (or 1) mm h^{-1}, PR_{fdp} was usually ~1.8 (>2) mm h^{-1}. For PR_{geo} <0.5 mm h^{-1}, PR_{fdp} was usually larger than PR_{geo}; this likely happened due to strong winds and turbulence. Figure 9g–i show PR_{tps}, PR_{geo}, and PR_{fdp} versus U_h, respectively. The PR_{tps} (box g) increases significantly with increasing U_h. Also, PR_{tps} was much larger than both PR_{geo} and PR_{fd12p} during strong wind conditions. Even if a trend were taken from Fig. 9g, PR_{tps} would be still larger than other PR values because it uses an internal algorithm to correct the PR. The PR_{geo} (box h) decreases with increasing U_h. The PR_{fdp} (box i) shows no strong wind dependency, and its maximum values were larger than PR_{geo}.

Figure 10a–f are obtained for T and RH_w, given along y axis, respectively. The T_{h45c} versus T_{h212}, T_{tps}, and T_{sr50} are shown in Fig. 10a. With increasing T, differences between any two increases. If we assume that T_{h45c} is correct and its value is −4 °C; the values of T_{tps}, T_{sr50}, and T_{h212} range from −5.0 °C to almost 0 °C. When T goes down to −6 °C, T values from all sensors are in the range of ±0.5 °C of the 1:1 line. Figure 10b shows T versus SWRF. When sun comes out, T measurements ranged between −6 and −5 °C (difference ~1 °C). This difference approached 5–6 °C when SWRF was 600 W m^{-2}. It seems that T_{h212} and T_{sr50} were less responsive to SWRF changes. Figure 10c shows T versus U_h where T_{tps} and T_{h45c} were significantly affected with increasing wind, resulting in lowering T from 2 to −2 °C, and from −2 to −4 °C, respectively. T_{tps} measurements were strongly affected by changing wind speed compared to other T measurements.

The RH_{wh212} versus RH_{wh45c} is shown in Fig. 10d. In this figure, for a given RH_{wh45c} ~90 %, RH_{wh212} varied by ~5 %. Uncertainty in RH_w increased to 10 % when it was ~70 %. Also, changing sign of RHw difference between two measurements was likely due to solar radiation effects shown on Fig. 10e where RH_w versus SWRF is plotted. For a given SWRF during sunrise, the difference between RHw_{h45c}, and RHw_{h212} was about 5 %. This uncertainty in RH_w during the afternoon was about 10–15 % when SWRF >350 W m^{-2}. The RH_w ranged between 70 and 100 % over U_h range (Fig. 10f). More data points close to 100 % RH_w suggest that saturation conditions exist usually when $U_h < 2$ m s^{-1}. RH_w becomes smaller when stronger winds occurred likely resulting in evaporative cooling.

4.2. Variability in the Measurements along the Mountain Slope

Variability in the measurements is studied using the three stations shown in Fig. 1. The RND, VOA,

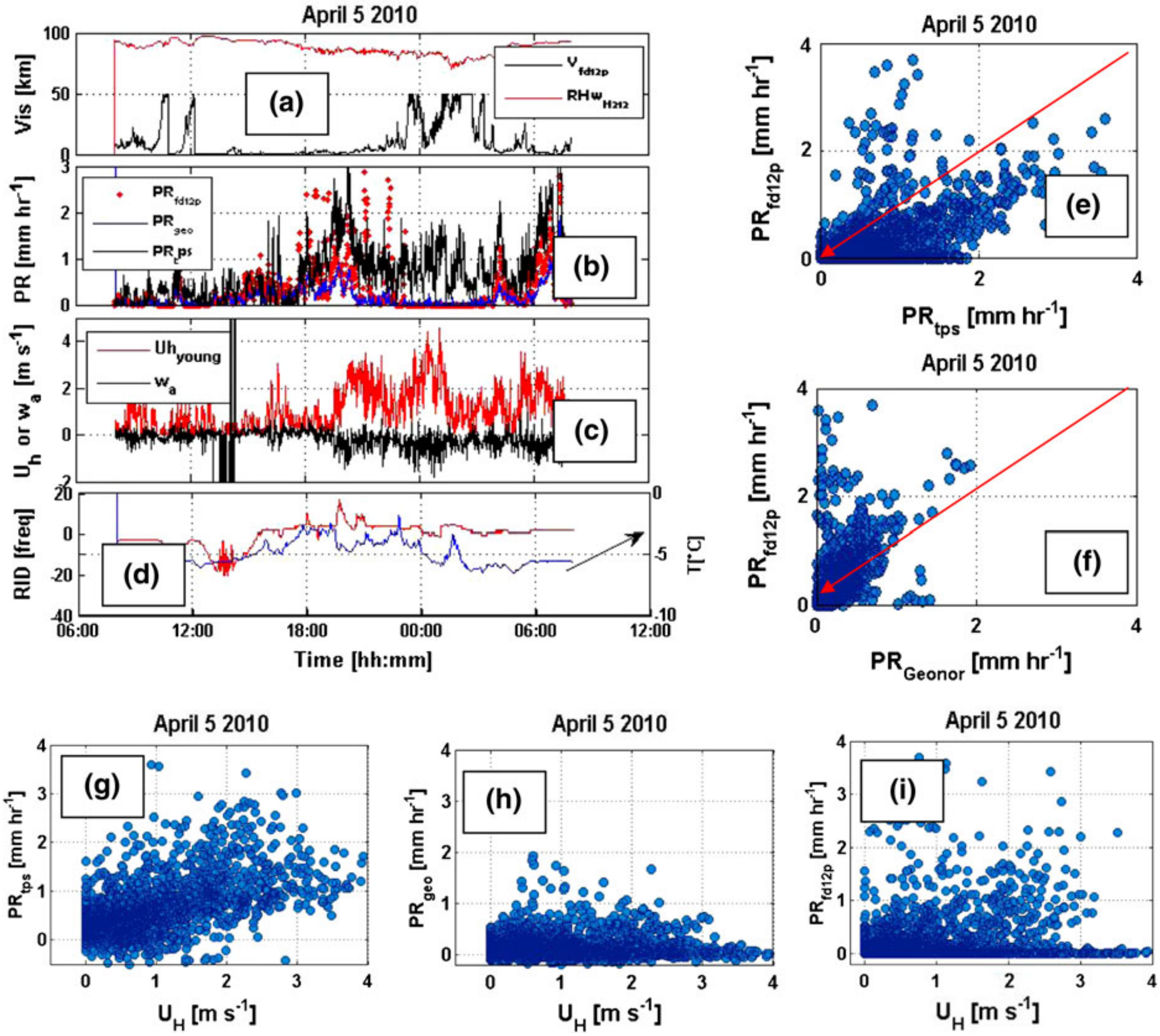

Figure 9
Time series and scatter plots of various measured parameters as given in Fig. 3 but they are for the April 5 2010 case

and VOL based FD12P measurements of Vis and PR, T, RH_w, and U_h are used to show the variability over 500 m along the slope from the VOL to RND. The mean and standard deviation (SD) values, and variability versus height (at the station level) are shown in Table 3 for the entire Feb 2010 period. Mo *et al.* (2012) and Gultepe and Zhou (2012) also showed that clouds along the mountain slope were not always linearly distributed and mid-mountain clouds were usually present while low and high levels were cloud free. Their work clearly demonstrated the horizontal and vertical variability. These results are discussed in the following section in the context of model verifications.

5. Discussions

5.1. Measurement Uncertainties

Uncertainty in the measurements at the RND site can be significant because of extreme weather conditions such as BSN, cold T, strong winds, and radiation effects. In this section, first we will

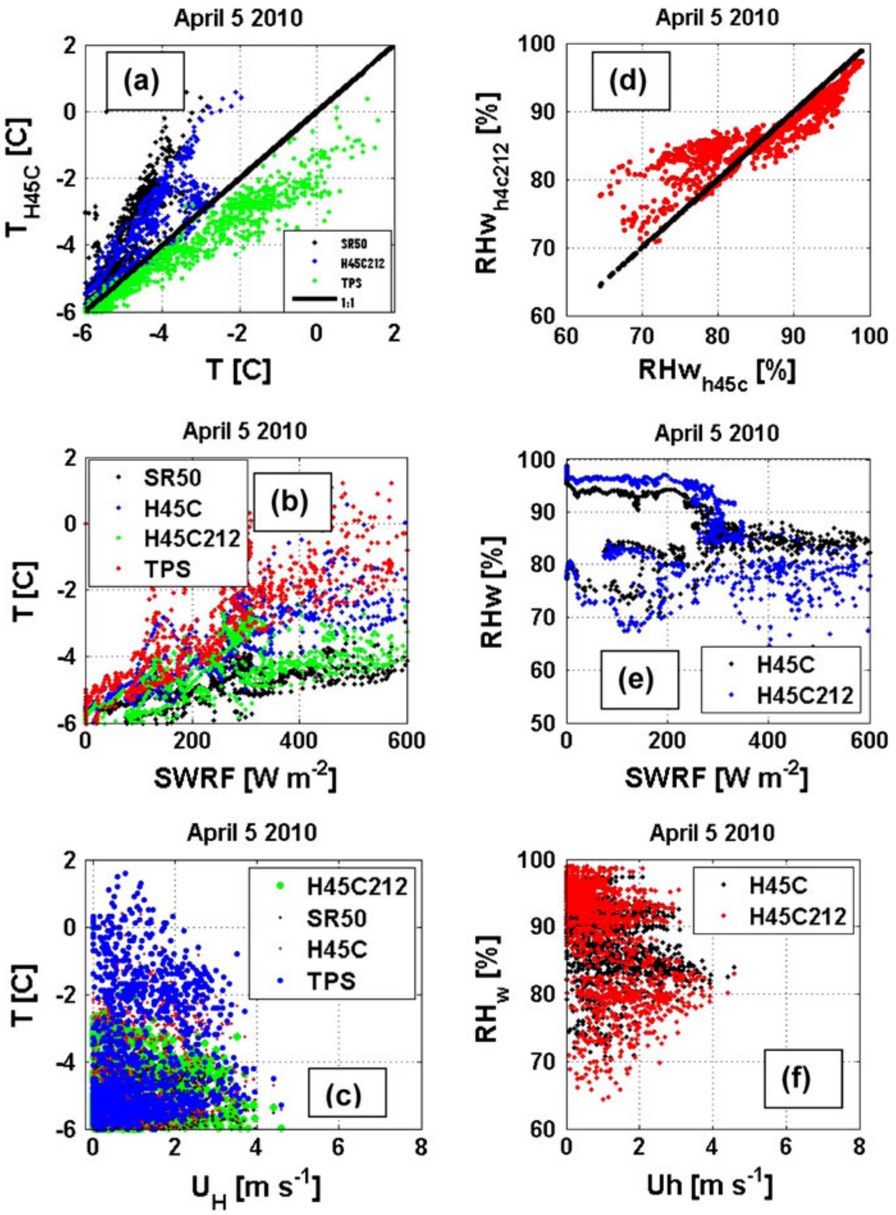

Figure 10
Scatter plots of temperature from HMP45C (T_{h45c}) versus others (T_{sr50}; T_{tps}; and T_{h45c}) (**a**), T_{h45c}, T_{h212}, and T_{tps} versus SWRF (**b**), T from all sensors versus horizontal wind speed (U_h) (**c**), RH_{wh212} versus RH_{w45c} (**d**), RH_{wh45c} versus short wave radiative flux (SWRF) (**e**), and RH_{w45c} and RH_{wh212} versus U_h (**f**) for April 5 2010

summarize the comparisons between HMP45C212 and HMP45C sensors (Table 1) from 20 days of randomly selected data for T and RH_w. The SWRF and wind effects on T and RH_w, comparisons of precipitation and Vis from various sensors, and the impact of w_a on PR are also given. In the end, the importance of averaging scales on the measured parameters, and their representativeness for model verification will be discussed.

5.1.1 *T and RH_w Comparisons*

The T and RH_w uncertainties for T down to −30 °C are usually given as +1 °C and 5 %, respectively, by the manufacturing companies. But these values can be much higher in extreme weather conditions (e.g. during mixed precipitation at ~ 0 °C; $T < -30$ °C; $U_h > 3$ m s^{-1}). Figure 11a, b show T and RH$_w$, respectively, obtained from HMP45C and HMP45C212 sensors as well as T from SR50 and TPS. The T comparisons using a randomly selected 20 days of data from December 1 2009 to April 5 2010 indicated that T differences significantly increase from $T = -13$ to $+1$ °C, and T_{tps} can be 2 °C larger than that of T_{h45c}. On the other hand, T_{h212} and T_{sr50} can be 2 °C colder than that of T_{h45c} at warm temperatures. Clearly, T uncertainty can be as high as 5 °C if we assume that T_{h45c} measurements are correct. Both H45C and H45C212 were calibrated at Vaisala Inc. The RH$_{wh45c}$ and RH$_{wh212}$ were plotted against each other in Fig. 11b. If RH$_{wh212}$ is fixed at 95 %, RH$_{wh45c}$ changes from 80 % up to 97 %, and the net change is $\sim$20 %. The percentiles and mean values are also shown on Fig. 11b. Overall, RH$_{wh212}$ are overestimated as compared to RH$_{wh45c}$.

5.1.2 SWRF and Wind Effects on T and RH$_w$

The SWRF can play an important role on T measurements because of the direct heating effect on the T sensor. Figure 11c shows T from various sensors (y axis) versus SWRF (x axis). It is obvious that SWRF may cause heating at the surfaces, resulting in an increase in T. When SWRF changes from 0 to 200 W m^{-2}, T change is about 1 °C. After 200 W m^{-2}, T values from all sensors became very noisy and with significant scatter being observed. Uncertainty in T was about ±3 °C because of changes in SWRF from 200 to 600 W m^{-2}. All T sensors respond similarly to SWRF changes. Note that early in the morning, the SWRF effect was about 2 °C. Figure 11d shows the effect of SWRF on RH$_w$ measurements. In reality, SWRF can affect RH$_w$ directly because, increasing SWRF may result in increasing moisture on the ground by melting the snow. Therefore, it is not easy to make firm conclusions on this issue. Figure 11d suggests that some accumulation of data points below 80 % may be related to SWRF heating problem and this is needed to be further analyzed.

Wind effects on T sensors are shown in Fig. 11e. In general, wind speed effects could not be identified clearly on T sensors but both T_{h212} and T_{h45c} were affected significantly with increasing wind speed when T is around 0 °C. This effect can be as high as 2 °C. Figure 11f shows w_a effect on PR$_{geo}$ and it is discussed in next subsection.

The SWRF and wind effects on T and RH$_w$ measurements are well known from many previous studies. A summary of radiation and wind effects on T and RH$_w$ is given by Huwald *et al.* (2009). They stated that over snow, 30 min mean T differences can be as large as 10 °C. Unshielded thermocouples were not affected as much as shielded ones for SWRF. They also stated that T errors decrease with decreasing solar radiative fluxes and increasing wind speed when a shield is used. The present work also suggested that SW heating effects can be as high 5 °C when T is close to 0 °C where diabatic effects can also be important. In our case, increasing wind speed resulted in an increasing error up to 3 °C in T measurements. Although it is not shown here, Huwald *et al.* (2009) stated that T measurement errors because of reflected SWRF increase much faster than incoming SWRF because of snow albedo effects. They used a sonic anemometer to improve the T measurements because its measurements are independent of SWRF. They also suggested a technique to improve the albedo effects and this will be considered for future studies.

5.1.3 3D Wind Effects on PR

Figure 11f shows the PR$_{geo}$ against w_a from the Young ultrasonic anemometer. This plot clearly shows that PR$_{geo}$ reaches its maximum value when $w_a \sim 0$ m s^{-1}. Increasing $+w_a$ suggests that air parcel goes away from the Geonor inlet, resulting in decreasing PR$_{geo}$. Increasing $-w_a$ also results in decreasing PR$_{geo}$. This result cannot be explained easily because increasing downward motions (see Eq. 1) should increase PR but this is not usually the case. This means that wind effects on precipitation can only be resolved by considering winds in 3D. Thériault *et al.* (2012) stated that snow gauge collection efficiency is also strongly related to snowflake characteristics. The results from the

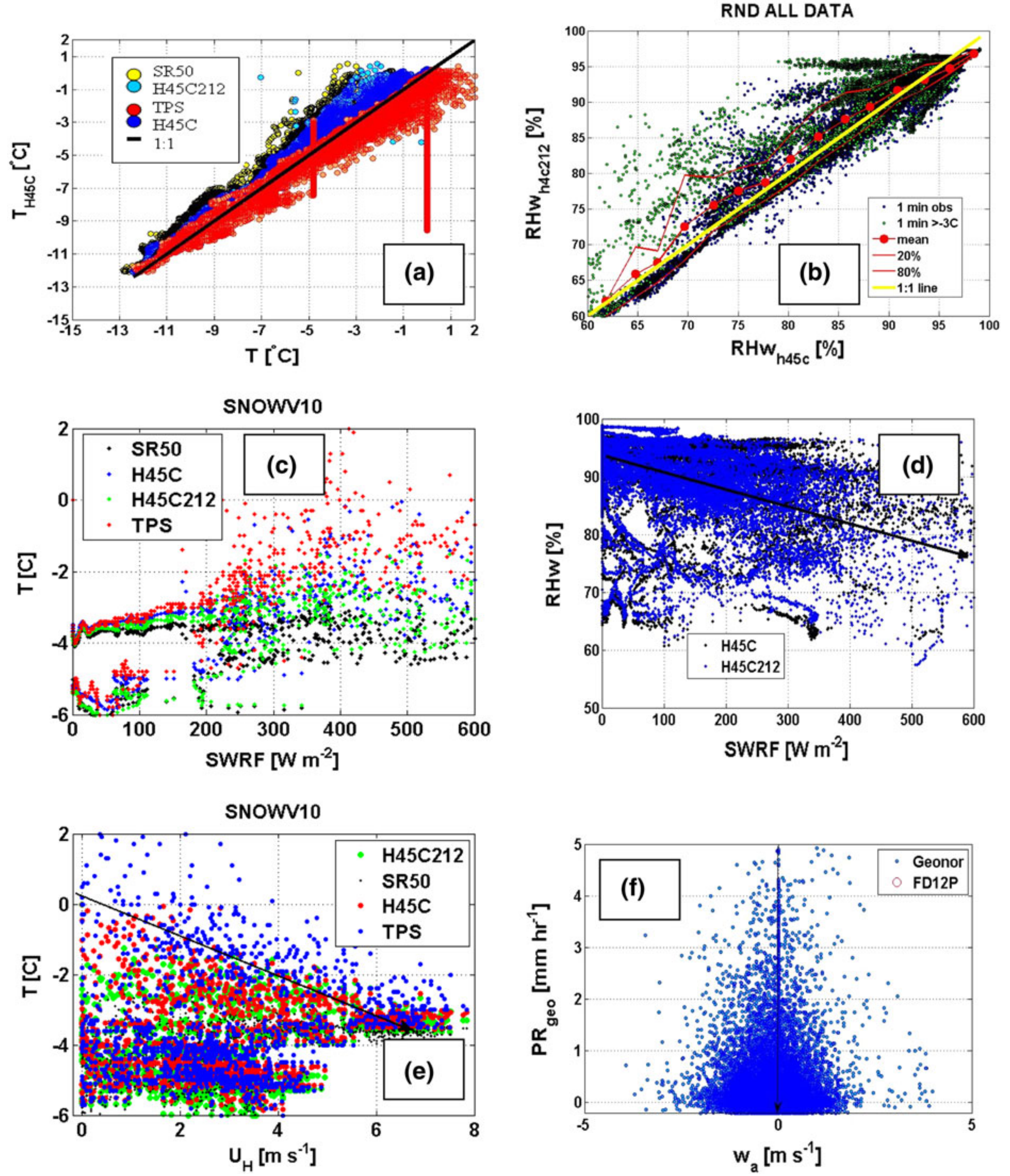

Figure 11

Scatter plots of temperature from HMP45C (T_{h45c}) versus others (T_{sr50}; T_{tps}; and T_{h45c}) (**a**) where solid line is for 1:1 line, $\mathrm{RH}_{\mathrm{wh212}}$ versus $\mathrm{RH}_{\mathrm{w45c}}$ (**b**) where *yellow line* is for 1:1 lines and mean with percentiles are also shown, T_{h45c}, T_{h212}, and T_{tps} versus SWRF (**c**), $\mathrm{RH}_{\mathrm{wh45c}}$ versus short wave radiative flux (SWRF) (**d**) where *solid line* is a trend line, T from all sensors versus horizontal wind speed (U_{h}) (**e**) where the *solid line* shows a possible trend on some data points, and $\mathrm{PR}_{\mathrm{geo}}$ versus w_{a} (**f**) for the randomly selected 20 cases from December 2009 to April 5 2010 current work suggest that a detailed flow model around the measuring gauges is needed to better assess the precipitation measurements quality.

5.1.4 PR Comparisons

The PR measurements during the project were collected at 1 min sampling rate. The PR measurements from the three transducers in the Geonor instrument are used to get instantaneous PR values after using 5 min running averages. Horizontal wind effects are not removed because of the lack of reference PR measurements. Also, it is shown that a correction cannot be made using only 2D winds (Fig. 11f). As shown during the case studies, increasing wind speed affects PR by decreasing its value. In ideal conditions, zero wind speed is perfect for accurate PR measurements. Therefore, horizontal wind effects can be taken away from the PR estimation algorithms. Figure 12a, b show PR_{fdp} versus PR_{tps} and PR_{geo}, respectively. Figure 12a shows that scattering increases with decreasing PR, and inconsistency is seen mostly for the low PR values. More scattering in PR_{fdp} versus PR_{geo} plot in Fig. 12b exists when PR is less than 1 mm h^{-1}. Clearly, when PR >2 mm h^{-1}, scattering of the data points decreases. Note that for a given value of PR_{fdp}, PR_{geo} and PR_{tps} can be two times more or less than PR_{fdp}.

5.2. Uncertainty and Variability in Vis

Visibility measurements are usually based on scattering and absorption properties of the particles in a small air volume nearby the transmitting and receiving sensors. Unfortunately, they don't represent the larger scales and their measurements are usually extended over tens of kilometers that may not represent variability. Variability (Var) here is defined as the ratio of SD to the mean (Var = SD/mean) for a given time and space scale. Especially over mountainous regions, real Vis may include much larger variability compared to those over smooth surfaces. Figure 6 previously showed that Vis may change quickly over a few minutes. Figure 12c shows Vis_{sen} versus Vis_{fdp} plot where a fit to data suggests that Vis_{fdp} is 1.5 times larger than Vis_{sen}. Also, increasing Vis results in larger scatter of the observations. Time series of Vis_{fdp} shown earlier suggested that Vis during snow and fog events may change drastically. Figure 9a as an example shows that Vis at about 1200 UTC drastically decreased from tens of kilometers down to a few hundreds of meters in less than a few minutes, suggesting that variability of Vis can be significant over very short time periods. Time series of PR measurements from different instruments are shown for various cases in Figs. 4, 6, 7, and 9. These showed that PR also changes quickly over periods of a few minutes, indicating that NWP models should represent microphysical processes over time periods less than a few minutes.

5.2.1 Vis versus Snow Type and Intensity at RND

The FD12P's particle shape recognition technique is a function of *T*, optical response to falling snow amount, and capacitance during the melting process. During the project, *T* between −3 and +6 °C was assigned to mixed phase precipitation based on the manufacturer's specifications. In that *T* range, as indicated earlier, *T* measurements may include large uncertainties that can affect the specification of snow type. Figure 12d shows the Vis versus PR obtained from the FD12P sensor as a function of snow type. The LSN, MSN, and HSN types are easily described using PR limits but other types of precipitation (see Fig. 12d) cannot be distinguished. Data points seen between Vis = 100 and 300 m for PR <1 mm h^{-1} may be related to light snow or ice crystals (e.g. snow grains, light ice pellets) but the same snow types are also seen between Vis = 2 and 10 km, suggesting that particle concentration was not determined accurately or snow type was not related to surface air *T*. A fit to all the data with 10 and 90 % lines is provided on the figure and its equation is obtained as

$$\mathrm{Vis[km]} = 2.432\mathrm{PR}^{-0.3684}[\mathrm{mm\,hr}^{-1}] - 1.16. \qquad (3)$$

This equation (with correlation coefficient $R = -0.65$) can be used for Vis estimation for snow PR but its percentile values should also be considered to get a probabilistic estimation of Vis (Gultepe and Milbrandt, 2010). Because of variability in Vis for a

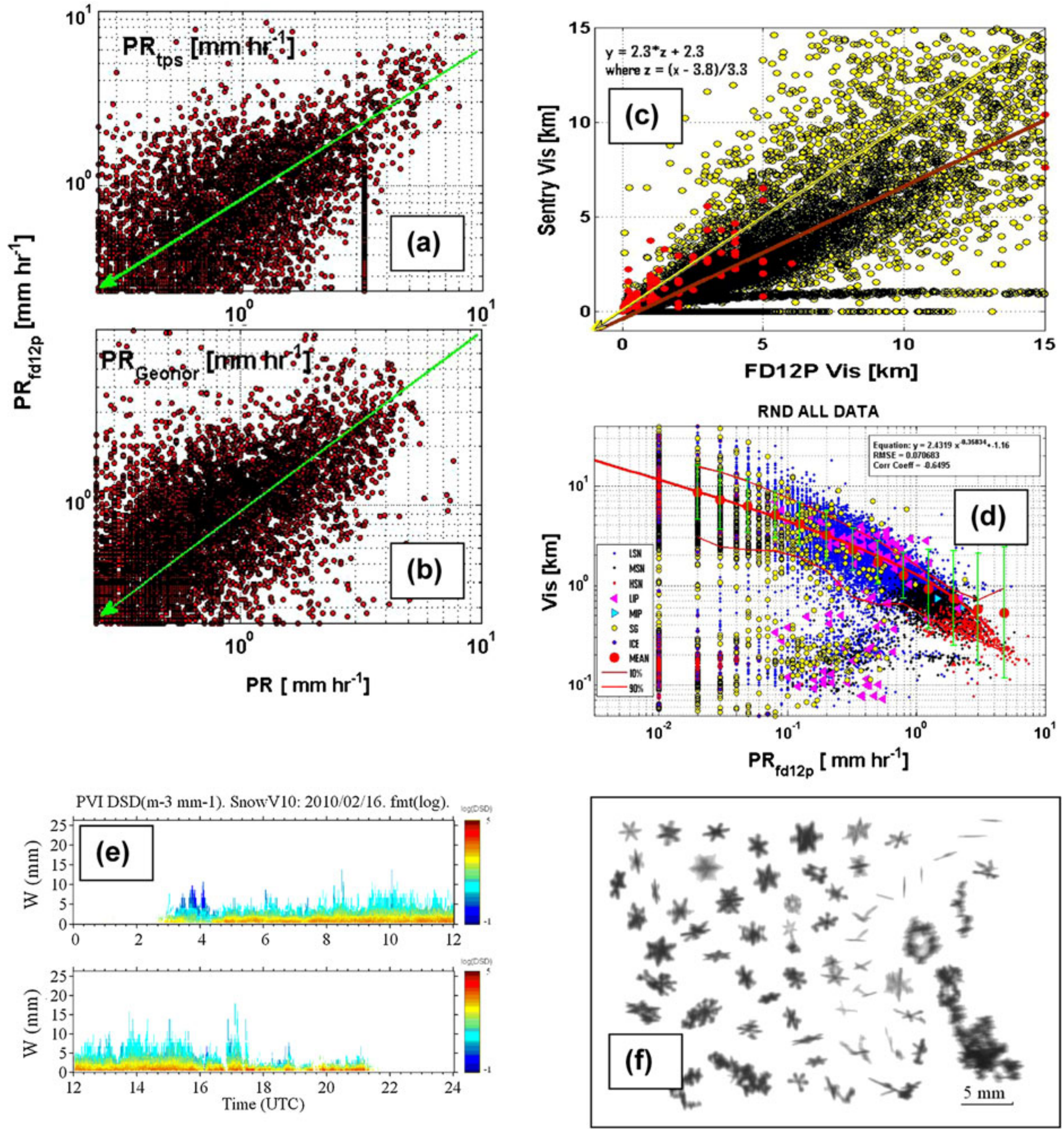

Figure 12

Scatter plot of PR$_{fdp}$ versus PR$_{tps}$ (**a**) and versus PR$_{geo}$ (**b**), Vis from sentry sensor (Vis$_{sen}$) versus Vis from FD12P (Vis$_{fdp}$) (**c**) where *red circles* are for human observations. The *red solid line* is a fit for all data points and yellow line is for 1:1 line. Scatter plot Vis$_{fdp}$ versus PR$_{fdp}$ for various snow types is shown in (**d**) where *red solid line* is for the fit to all data points (equation is given on the plot). The mean (*red filled circles*) and percentiles (*red thin lines*) as well as SD bars (*green lines*) are also shown on (**d**) for all 20 cases. The labels of LSN, MSN, HSN, LIP, MIP, SG, ICE, MEAN, 10 and 90 % represent, respectively, light snow, medium snow, heavy snow, light ice pellet, medium ice pellet, snow grain, ice crystals, mean, 10 and 90 % percentiles. Time series of width (W) of the particles measured with a PVI are shown in (**e**) where the *color bar* indicates the particle number concentration density log(N_{id}). The ice crystal images, showing the variability of the shapes, collected during the snow storm at the RND station are shown in (**f**) for February 16 2010 given PR value, we should not compare the fit values to mean values simulated with a forecasting model.

5.2.2 *Variability in Snow Particle Type and Intensity at RND*

Snow precipitation rate is directly related to snow particle types and their fall speed (which is also related to density). As shown in Fig. 2, snow crystal types can change significantly over 1 min time periods. Using the PVI sensor (Newman *et al.*, 2009), time series of snow crystal width (W) are shown in Fig. 12e; the color bar shows the spectral concentration density (N_{id}) of snow crystals. Clearly, for $W < 1$ mm, N_{id} becomes about 5 m^{-3} mm^{-1}. Figure 12f shows the snow crystal shapes from PVI; including columns/needles, dendrites, sector plates, and aggregates with sizes up to 5 mm. Equation 1 suggests that V_f which is function of particle shape and density plays a significant role in the PR calculation.

5.2.3 *Variability along the Slope: Daily 1-min Observations*

The observations collected during SNOW-V10 created a unique data set to study variability over the

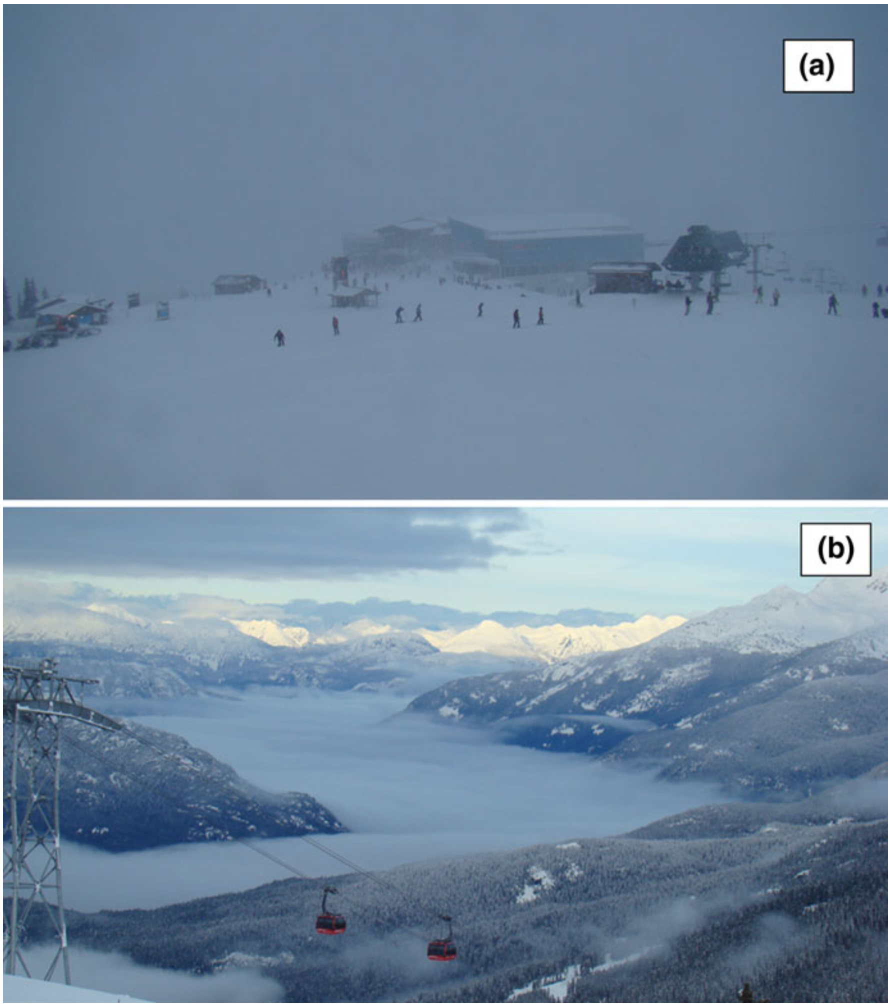

Figure 13
Variability in the weather conditions on Jan 17 2010: snowing at the RND site (1,853 m) at 1000 LST (**a**) and fogy/cloudy below the RND site at the VOA and VOL sites on 1600 LST (**b**). The fog/cloud filled the valley below the RND site on this day

Whistler Mountain slope. The Jan 17 2010 case is chosen as an example to show the variability along the Whistler Mountain. Figure 13 shows two pictures representing the weather conditions at 1000 LST (snowing 1800 UTC) and 1600 LST (fogy). The five stations were located along the slope but only three of them are used for discussions here. The observations of Vis and PR (from FD12P), T, RH_w, and wind speed/direction were collected at each minute. Figure 14 shows the time series of Vis, PR, T, RH_w, and wind speed from RND, VOA, and VOL stations to indicate variability over a distance about 500 m. Box (a) shows that Vis ranges from 100 m to 10 km depending on the stations at 1800 UTC. During snow precipitation (box b), Vis differences can be more than 1 km (1200 UTC). Snow PR_{fdp} at 0200 UTC ranges from 0.5 mm h^{-1} (VOL) up to 3 mm h^{-1} (RND). The U_h ranges from 1 m s^{-1} (VOL) to 7 m s^{-1} (VOA) at 1100 UTC (box c). During saturation (foggy) conditions, RH_w becomes very close to 100 % at all stations except during clear air conditions (from 0000 to 0400 UTC), where differences between stations are about 40 % (box d). Absolute T differences become more than 3 °C during clear air conditions (box e) and ~1 °C when snowing at the all stations.

5.2.4 *Variability along the Slope: Monthly Averaged 1-min Observations*

Variability in the measurements is studied using the data collected at the three stations shown in Fig. 1. The RND, VOA, and VOL based FD12P measurements of Vis and PR are used to show the variability over ~500 m height in the vertical (700 m

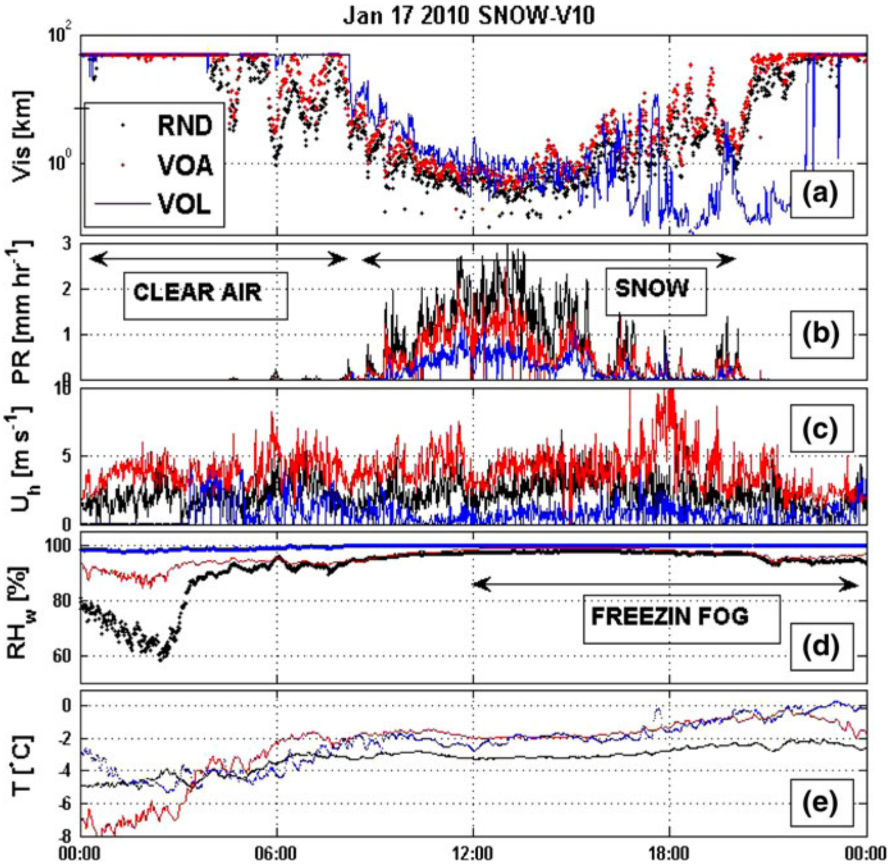

Figure 14

Time series of Vis (**a**), PR (**b**) from FD12P, U_h from 3D ultrasonic anemometer (**c**), RH_{wh45c} (**d**), and T_{h45c} (**e**) for RND, VOA, and VOL sites to show the vertical variability over along a 500 m slope for Jan 17 2010 along the slope) from the station VOL to RND. Table 3 shows the monthly mean, SD, and variability (SD/mean) of the 1 min observations in February 2010 from the individual stations along the slope. In fact, differences between two stations represent the scale of about 200 m. The results show that MRV (maximum relative variability) for PR, Vis, T, RH$_w$, and U_h over February 2010 can be up to 43 %, 73 %, 140 %, 10 %, and 76 % (Table 3), respectively, along the 700 m slope. This result can contribute to a significant error in comparisons with NWP models when a forecasting model has a resolution of about 1 km in the horizontal and 100 m in the vertical. Bailey *et al.* (2012) showed that both RND and VOA sites share the same GEM-REG-15 km and GEM-LAM-1 km model points; therefore, comparisons become difficult unless models resolved these scales. Note that individual variability of the parameters at each station can be up to 100 % per minute except for RH$_w$ (which is up to 30 %). The RH$_w$ measurements can be highly susceptible to measurement errors as described earlier. Further analysis of the observations on this issue will be made later using extended data sets from the stations along the slope (Fig. 1).

6. Conclusions

The main conclusions obtained from this work are important for nowcasting PR, Vis, T, RH, and U_h using forecast models, and for their verifications using statistical methods and observations. The meteorological parameters can change quickly over short time and space scales as described. The models should have enough time and space resolutions to reduce the scale dependent uncertainties. For example, vertical (horizontal) space resolutions of the forecasting models should be better than 50 m. Otherwise, because of variability, comparisons using point observations may not be accurate, resulting in large uncertainty issues. The main points obtained from this work can be summarized as:

Table 3

Mean, SD, variability (var), 10 %, 50 %, and 90 % values of FD12P PR, Vis, T, RH$_w$, and U$_h$ over entire Feb 2010 based on 1 min observations. FD12P PR threshold used was 0.05 mm hr^{-1} to account for light precipitation. Last two rows are for absolute MDM (maximum difference of means) and maximum relative variability (MRV = MDM/max mean) for all cases

RND	PR (mm h^{-1})	Vis (km)	T (°C)	RH$_w$ (%)	U_h (m s^{-1})
Mean/SD	0.53/0.64	3.18/0.77	−2.82/1.22	92.91/5.11	1.59/1.22
Var	1.21	1.18	0.43	0.06	0.77
10 %; 50 %; 90 %	0.03/0.29/1.33	0.53/2.01/6.98	−4.35/−2.86/−1.18	87.20/93.60/97.80	0.25/1.34/3.24
VOA	PR	Vis	T	RH$_w$	U_h
Mean/SD	0.31/0.35	3.79/3.67	−1.71/1.45	84.33/26.42	2.17/1.55
Var	1.14	0.97	0.85	0.31	0.71
10 %; 50 %; 90 %	0.03/0.19/0.72	0.72/2.57/8.39	−3.67/−1.76/0.10	75.60/93.40/98.20	0.40/1.87/4.41
VOL	PR	Vis	T	RH$_w$	U_h
Mean/SD	0.30/0.33	2.53/3.21	−0.79/0.88	90.37/27.32	1.08/0.98
Var	1.13	1.27	1.11	0.30	0.91
10 %; 50 %; 90 %	0.03/0.20/0.64	0.15/1.58/6.17	−1.93/−0.72/0.21	90.30/99.90/100	0.04/0.79/2.56
VOT	PR	Vis	T	RH$_w$	U_h
Mean/SD	0.40/0.59	9.49/10.50	1.11/0.09	92.75/23.18	0.51/0.47
Var	1.48	1.10	0.89	0.25	0.92
10 %; 50 %; 90 %	0.04/0.25/0.84	1.42/5.70/22.78	0.11/0.82/2.58	90.19/100/100	0.04/0.39/1.14
MDM	0.23	6.96	3.93	9.00	1.66
MRV	(43 %)	(73 %)	(140 %)	(10 %)	(76 %)

1. Time and space variability obtained from surface point observations can be significant and they may not be compared directly with NWP simulations.
2. Models need better subgrid scale representation of the processes to resolve smaller scales (e.g. <100 m).
3. Uncertainties in RH_w and T because of wind and SWRF variations can be as high as 20 % and 2–3 °C, respectively.
4. Vertical air velocity (w_a) can increase or decrease PR depending on U_h direction, suggesting that 3D winds need to be used in improving snow PR measurements.
5. TPS measurements are strongly affected by the horizontal wind speed, and resulted in up to 100 % error in PR when a collection efficiency equation used in the embedded algorithm.
6. FD12P measurements were not affected by the wind as much as TPS and Geonor measurements, and it was the best sensor for mountain applications to record the precipitation rate (especially for rates <0.5 mm h^{-1}). PR from Geonor and TPS was usually found to be strongly affected by wind speed.
7. Snow type changed drastically over 1 min time periods in many conditions, and the FD12P was a good sensor for distinguishing snow fall rate as light, medium, and heavy, but was not a good indicator for individual ice crystal shape recognition.
8. LPM sensor was overestimating PR but it was good for BSN detection and snow type.
9. Uncertainty in Vis from both FD12P and Sentry can be significant for both low and high Vis conditions, and also from human based observations.
10. Variability over 700 m scale along a mountain slope can be up to 100 % for many meteorological parameters; therefore, observations and models should have similar time and space scale resolutions for comparisons.
11. Based on observational uncertainties, additional methods and efficient project setups should be developed for model validations.

This work suggested that PR, Vis, T, and RH_w measurements need to be improved over the complex terrain; also, other than point measurements, some areal based techniques should be developed for model validations. Future work on this issue using SNOW-V10 observations will be considered.

Acknowledgments

The authors wish to thank the support of the World Weather Research Program (WWRP) of the World Meteorological Organization (WMO) and specifically the Nowcasting Working Group of WWRP and Environment Canada. Additional support was provided by the SAR Office by funding the FRAM (Fog Remote Sensing and Modeling) project to study fog over various environmental conditions. Authors also thank to technicians: Steve Bacic, Mike Harwood, Ben Underhill, and R. Reed, for maintaining and calibrating instruments during harsh weather conditions at the Whistler Mountain RND site at 1,856 m.

Appendix

The symbols and definitions used in the text are defined below:

BSN	Blowing snow
C_i	Snow crystal counts
DS	Now crystal diameter
FF	Freezing fog
FDRZ	Freezing drizzle
HSN	Heavy snow
ICNG	Icing
LWC	Liquid water content
LSN	Light snow
MSN	Medium snow
N_i	Snow crystal number concentration
N_{id}	Snow crystal number density
PR_{geo}	Precipitation rate from Geonor instrument
PR_{fdp}	Precipitation rate from FD12P instrument
PR_{tps}	Precipitation rate from TPS instrument
RH_w	Relative humidity with respect to water
RH_{wh212}	Relative humidity from Vaisala HMP45C212 sensor
RHw_{h45c}	Relative humidity from Vaisala HMP45C sensor

SA	Sampling area
SN	Snow
SWE	Snow water equivalent
SWRF	Broadband shortwave radiative flux
Δt	Sampling period
T	Temperature
T_{h45c}	Temperature from Vaisala HMP45C sensor
T_{h212}	Temperature from Vaisala HMP45C212 sensor
T_{tps}	Temperature from TPS sensor
T_{sr50}	Temperature from SR50 sensor
U_{h}	Horizontal wind
V_{f}	Snow crystal fall velocity
Vis	Visibility
$\mathrm{Vis}_{\mathrm{sen}}$	Visibility from sentry sensor
$\mathrm{Vis}_{\mathrm{fdp}}$	Visibility from FD12P sensor
W	Snow crystal width
w_{a}	Vertical air velocity

Station Names

RND	Roundhouse site
VOA	Whistler Mountain high level site
VOL	Whistler Mountain mid-level site
VOT	Whistler Mountain timing flat site
TFT	Whistler timing flat site
VOC	Nesters station site

Models and Project Names

NWP	Numerical weather Prediction
GEM-REG	The Global Environment Multiscale Model with 15 km resolution
GEM-LAM	High-resolution limited-area model version of the GEM with 1.5 km
FRAM-IF	Fog Remote Sensing and Modeling-Ice Fog project
SNOW-V10	Science of Nowcasting Winter Weather for the Vancouver 2010 Olympics and Paralympics

REFERENCES

Bailey, M.E., G.A. Isaac, I. Gultepe, I. Heckman and J. Reid, (2012), *Adaptive Blending of Model and Observations for Automated Short Range Forecasting: Examples from the Vancouver 2010 Olympic and Paralympic Winter Games*. Pure and Applied Geophysics. doi:10.1007/s00024-012-0553-x.

Bianco, L., Domenico Cimini, Frank S. Marzano, and Randolph Ware, (2005), *Combining Microwave Radiometer and Wind Profiler Radar Measurements for High-Resolution Atmospheric Humidity Profiling*. Journal of Atmospheric and Oceanic Technology. V. *22*, Issue 7, 949-965.

Brandes, Edward A., Kyoko Ikeda, Guifu Zhang, Michael Schönhuber, Roy M. Rasmussen, (2007), *A Statistical and Physical Description of Hydrometeor Distributions in Colorado Snowstorms Using a Video Disdrometer*. J. Appl. Meteor. Climatol., *46*, 634–650.

Goodison, B. E., B. Sevruk, and S. Klemm, (1989), *WMO solid precipitation measurement intercomparison: Objectives, methodology, analysis.* Atmospheric Deposition Proc. Baltimore Symp., Baltimore, MD, IAHS, 57–64.

Gultepe, I., and B. Zhou, (2012), *The fog to snow conversion process during winter Olympic Project*, J. Pure and Appl. Geophy., vol. *169*, N.6/8, 2012, 300 pp.

Gultepe, I., T. Kuhn, M. Pavolonis, C. Calvert, J. Gurka, A. J. Heymsfield, P.S.K. Liu, B. Zhou, R. Ware, B. Ferrier, J. Milbrandt, B. Hansen, and B. Bernstein, (2012), *Ice fog (pogonip) in Arctic during FRAM-IF project: Aviation and nowcasting applications.* AMS Bulletin. Accepted.

Gultepe, I., and J. A. Milbrandt, (2010), *Probabilistic Parameterizations of Visibility Using Observations of Rain Precipitation Rate, Relative Humidity, and Visibility*. J. Appl. Meteor. Climatol., *49*, 36–46.

Gultepe, I., G. Pearson J. A. Milbrandt, B. Hansen, S. Platnick, P. Taylor, M. Gordon, J. P. Oakley, and S.G. Cober, (2009), *The fog remote sensing and modeling (FRAM) field project.* Bull. Of Amer. Meteor. Soc., v.*90*, 341-359.

Gultepe, I., and Starr, D. O'C., (1995), *Dynamical structure and turbulence in cirrus clouds: Aircraft observations during FIRE.* J. Atmos. Sci., *52*, 4060-4078.

Huang, Gwo-Jong, V. N. Bringi, Robert Cifelli, David Hudak, W. A. Petersen, 2010: *A Methodology to Derive Radar Reflectivity–Liquid Equivalent Snow Rate Relations Using C-Band Radar and a 2D Video Disdrometer*. J. Atmos. Oceanic Technol., *27*, 637–651.

Huwald, H., C. W. Higgins, M. O. Boldi, E. Bou-Zeid, M. Lehning, and M. B. Parlange, 2009: *Albedo effect on radiative errors in air temperature measurements*. Water Res. Res., *45*, W08431, doi:10.1029/2008WR007600. 13 pp.

Isaac, G.A., P. Joe, J. Mailhot, M. Bailey, S. Bélair, F.S. Boudala, M. Brugman, E. Campos, R.L.Carpenter Jr., R.W.Crawford, S.G. Cober, B. Denis, C. Doyle, H.D. Reeves, I.Gultepe, T. Haiden, I. Heckman, L.X. Huang, J.A. Milbrandt, R. Mo, R.M. Rasmussen, T. Smith, R.E. Stewart, D. Wang and L.J. Wilson, 2012: *Science of Nowcasting Olympic Weather for Vancouver 2010 (SNOW-10): A World Weather Research Programme project*. Pure and Applied Geophysics. doi:10.1007/s00024-012-0579-0

Joe, P., Bill Scott, C. Doyle, G. Isaac, I. Gultepe, D. Forsyth, S. Cober, E. Campos, I. Heckman, N. Donaldson, D. Hudak, R. Rasmussen, R. Stewart, J. M. Thériault, H. Carmichael, M. Bailey and F. Boudala, 2012: *The Monitoring Network of the Vancouver 2010 Olympics*. Pure and Applied Geophyiscs. doi: 10.1007/s00024-012-0588-z.

Mailhot, J., J.A. Milbrandt, A. Giguère, R. McTaggart-Cown, A. Erfani, B. Denis, A. Glazer and M. Vallée, (2012), *An experimental high-resolution forecast system during the Vancouver 2012 Winter Olympic and Paralympic Games*. Pure and Applied Geophysics. doi:10.1007/s00024-012-0520-6.

Mo, Ruping, Paul Joe, George A. Isaac, Ismail Gultepe, Roy Rasmussen, Jason Milbrandt, Ron McTaggart-Cowan, Jocelyn Mailhot, Melinda Brugman, Trevor Smith, and Bill Scott, (2012), *Mid-mountain clouds at Whistler during the Vancouver 2010 Winter Olympics and Paralympics*. Pure and Applied Geophysics. doi:10.1007/s00024-012-0540-2.

Newman, A. J., Paul A. Kucera, and Larry F. Bliven, (2009), *Presenting the Snowflake Video Imager (SVI)*. Journal of Atmospheric and Oceanic Technology. V *26*, 2 167-179.

Rasmussen, R.M., John Hallett, Rick Purcell, Scott D. Landolt, and Jeff Cole, 2011: *The Hotplate Precipitation Gauge*. Journal of Atmospheric and Oceanic Technology. V. *28*, 148-164.

Thériault, J. M., R. Rasmussen, K. Ikeda, and S. Landolt (2012) *Dependence of snow gauge collection efficiency on snowflake characteristics*. J. Appl. Meteor. and Clim.,*51*,745-762.

Thériault, J. M., K. L. Rasmussen, T. Fisico, R. E. Stewart, P. Joe, I. Gultepe, M. Clément and G. A. Isaac (2012) *Weather Observations Along Whistler Mountain in Five Storms During SNOW-V10*. Pure and Applied Geophysics. doi:10.1007/s00024-012-0590-5.

WMO/CIMO, (1985), *International Organizing Committee for the WMO Solid Precipitation Measurement Intercomparison,* Final Report of the first session. WMO Rep., 31 pp.

Yang, D., B. E. Goodison, J. R. Metcalfe, V. S. Golubev, R. Bates, T. Pangburn, and C. L. Hanson, (1998), *Accuracy of NWS 8″ standard nonrecording precipitation gauge: Results and applications of WMO intercomparison*. J. Atmos. Oceanic Technol., *15*, 54–68.

Yang, D., and Coauthors, (2001), *Compatibility evaluation of national precipitation gage measurements*. J. Geophys. Res., *106*, (D2). 1481–1491.

(Received March 29, 2012, revised June 18, 2012, accepted July 18, 2012, Published online November 16, 2012)